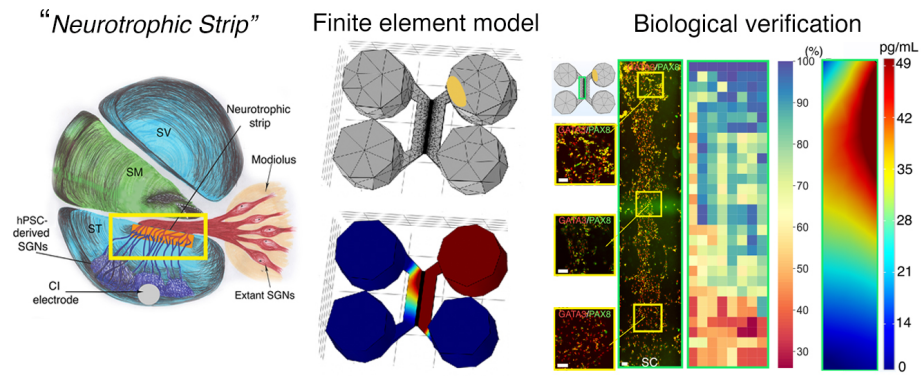


# Graphical Abstract

## Developing the Bioactive Cochlear Implant: Bridging the electrode–neuron gap through neurite guidance

Kevin T. Nella, Benjamin M. Norton, Hsiang-Tsun Chang, Rachel A. Heuer,  
Christian B. Roque, Akihiro J. Matsuoka



# Developing the Bioactive Cochlear Implant: Bridging the electrode–neuron gap through neurite guidance

Kevin T. Nella<sup>a,b</sup>, Benjamin M. Norton<sup>a</sup>, Hsiang-Tsun Chang<sup>a</sup>, Rachel A. Heuer<sup>a</sup>, Christian B. Roque<sup>a</sup>, Akihiro J. Matsuoka<sup>a,c,d,e,\*</sup>

<sup>a</sup>*Department of Otolaryngology–Head and Neck Surgery, Feinberg School of Medicine, Northwestern University, Chicago IL, 60611, USA*

<sup>b</sup>*Department of Mechanical Engineering, Robert R. McCormick School of Engineering and Applied Science, Northwestern University, Evanston, IL., USA*

<sup>c</sup>*Simpson Querrey Institute, Chicago IL, 60611, USA*

<sup>d</sup>*Roxelyn and Richard Pepper Department of Communication Sciences and Disorders, School of Communication, Northwestern University, Evanston, IL., 60210, USA*

<sup>e</sup>*The Hugh Knowles Center for Clinical and Basic Science in Hearing and its Disorders, Evanston, IL. 60210, USA*

---

## Abstract

Although cochlear implant (CI) technology has allowed partial restoration of hearing over the last few decades, persistent challenges remain - including the deciphering of rich acoustic signals into a digital pulse-train signal. Among these challenges, the “electrode–neuron gap” poses the most significant obstacle to advancing past the current plateau in CI performance. Resulting issues include limited performance in noisy environments and a poor ability to decode intonation and music. We propose the development of a “neurotrophic strip”—a biological interface that doubly preserves endogenous spiral ganglion neurons (SGNs) while precisely directing the growth of neurites arising from transplanted human pluripotent stem cell (hPSC)-derived otic neuronal progenitors (ONPS), toward endogenous SGNs. We hypothesized that the Polyhedrin Delivery System (PODS®-human brain-derived neurotrophic factor [BDNF]) could stably

---

\*Corresponding author: Akihiro J. Matsuoka, Department of Otolaryngology–Head and Neck Surgery, Feinberg School of Medicine, Northwestern University, 676 North St. Clair Street Suite 1325, Chicago, IL 60611, USA. E-mail addresses: amatsuok@nm.org, akihiro.matsuoka@northwestern.edu.

Email addresses: kevin.nella@northwestern.edu (Kevin T. Nella), benjamin.norton@northwestern.edu (Benjamin M. Norton), hsiangtsun.chang@gmail.com (Hsiang-Tsun Chang), racheuer@gmail.com (Rachel A. Heuer), christian.b.roq@gmail.com (Christian B. Roque), amatsuok@nm.org (Akihiro J. Matsuoka)

provide an adequate BDNF gradient to hPSC-derived ONPs, thereby simultaneously facilitating otic neuronal differentiation and directional neurite outgrowth. To test this hypothesis, we first devised a finite element model to simulate the *in vitro* BDNF gradient generated by PODS®. For biological verification, we validated the concept of the neurotrophic strip by using a multi-chamber microfluidic device, which mimics the *in vivo* micro-environment more accurately than conventional laboratory plates in terms of volume and concentrations of endogenous/exogenous factors. We were able to generate the optimal BDNF concentration gradient to enable survival, neuronal differentiation toward hPSC-derived SGNs, and directed neurite extension of hPSC-derived SGNs. The technique will allow us to further advance our concept of the “neurotrophic strip” by controlling neurite direction of transplanted hPSC-derived ONPs. This proof-of-concept study provides a step toward the next generation of CI technology.

*Keywords:* human pluripotent stem cells, finite element model, microfluidic device, neurotrophic factor, cochlear implant, neuroelectric interface, stem cell niche, spiral ganglion neurons

*2010 MSC:* 74S05, 62P10, 92C20

---

<sup>1</sup> **1. Introduction**

<sup>2</sup> The cochlear implant (CI), which provides functional restoration in patients  
<sup>3</sup> with sensorineural hearing loss, forms a neuro-electronic interface with the pe-  
<sup>4</sup> ripheral auditory nervous system [1]. CI technology functions by electrically  
<sup>5</sup> stimulating the extant population of auditory neurons (i.e., spiral ganglion neu-  
<sup>6</sup> rons [SGNs]). Although CI technology has allowed partial restoration of hearing  
<sup>7</sup> for this patient population over the last few decades, persistent challenges, in-  
<sup>8</sup> cluding the deciphering of rich acoustic signals into digital pulse-train signals,  
<sup>9</sup> remain. Among these challenges, the “electrode-neuron gap” poses the most  
<sup>10</sup> significant obstacle to advancing past the current plateau in CI performance.  
<sup>11</sup> This phenomenon results in limited performance in noisy environments and poor  
<sup>12</sup> ability to decode intonation and music [2], arguably decreasing quality of life.  
<sup>13</sup> The gap exists between the CI electrode and the target membranes of dendrites  
<sup>14</sup> in surviving endogenous SGNs [3]. It results in the requirement of larger CI  
<sup>15</sup> excitation fields, leading to current spread that excites and therefore disables  
<sup>16</sup> the neighboring electrodes, resulting in fewer information channels to the brain,  
<sup>17</sup> all within discrete time steps [2, 4]. This can develop into a vicious cycle as  
<sup>18</sup> fewer information channels to the brain also prompt the need for larger CI ex-  
<sup>19</sup> citation fields. The length of the gap generally spans hundreds of  $\mu\text{m}$  [5, 6].  
<sup>20</sup> Hahnewald et al. demonstrated *in vitro* that energy needed to elicit a response  
<sup>21</sup> can be reduced by up to 20% by reducing the distance from 40 to zero  $\mu\text{m}$  (by  
<sup>22</sup> growing early postnatal mouse SGN explants on a microelectrode array) [4].

<sup>23</sup> To resolve the electrode-neuron gap *in vivo*, previous work has introduced  
<sup>24</sup> the concept of a bioactive CI (Figure. 1A) [7, 8, 9]. The bioactive CI combines  
<sup>25</sup> the current state-of-the-art CI technology with emerging stem cell-replacement  
<sup>26</sup> therapy in the inner ear. In this scheme, transplanted human pluripotent stem  
<sup>27</sup> cell (hPSC)-derived SGNs bridge the gap between the CI electrode and sur-  
<sup>28</sup> viving endogenous SGNs. Neurotrophin gradients have been shown to guide  
<sup>29</sup> hPSC grafts in spinal cord injury [10], direct growth of endogenous SGNs to-  
<sup>30</sup> ward CI electrodes in the scala tympani [11], and enable transplanted hPSC

31 derived otic neuronal progenitors (ONPs) to grow neurites toward the modiolus  
32 [9]. Although promising, these studies failed to observe adequate directional  
33 neurite outgrowth toward endogenous SGNs (i.e., lack of synaptic connections  
34 between hPSC grafts and endogenous SGNs), presumably preventing significant  
35 improvements in functional recovery of hearing.

36 To confront this issue, we propose the development of a “neurotrophic strip”—a  
37 biological interface that doubly preserves endogenous SGNs while precisely di-  
38 recting the growth of neurites arising from transplanted hPSC-derived ONPs  
39 toward the endogenous SGNs. The highlighted yellow-square area in Figure  
40 1A shows a schematic diagram of this concept. Here, the neurotrophic strip  
41 (shown as an orange rectangle in Figure 1A) stimulates neurite outgrowth from  
42 both the hPSC-derived ONPs and the endogenous SGNs via a neurotrophic fac-  
43 tor gradient [12]. While the concept of a neurotrophin gradient for directional  
44 axonal growth has existed for a few decades, incorporating neurotrophin gradi-  
45 ents into any tissue-engineered scaffold has been extremely challenging due to  
46 the lack of self-sustaining neurotrophin delivery methods—their eventual deple-  
47 tion triggers an accelerated decline in neurite growth and the survival of extant  
48 SGNs [13, 14, 15]. One major contributor is the structurally unstable nature of  
49 neurotrophins, which suffer from fragility and thermo-instability under normal  
50 physiological conditions both *in vitro* and *in vivo*, leading to short half-lives typi-  
51 cally ranging from minutes to hours [16]. This issue can be overcome by utilizing  
52 the polyhedrin delivery system (PODS®)—a crystalline growth factor formu-  
53 lation developed to enable long-term release of growth factors while dampening  
54 degradation rates at the source [17, 18, 19] (Figure 1B). The PODS® technology  
55 has adapted viral machinery to encase a chosen growth factor into polyhedrin  
56 protein cases. The resultant growth factor co-crystals have slow degradation pro-  
57 files under physiological conditions and, therefore, allow the sustained release of  
58 embedded bioactive growth factor protein such as neurotrophins.

59 We reasoned that an bio-engineered scaffolding incorporated with PODS®  
60 technology can establish a neuronal network between transplanted hPSC-derived  
61 ONP grafts and extant SGNs in the inner ear. More specifically, we hypothesized

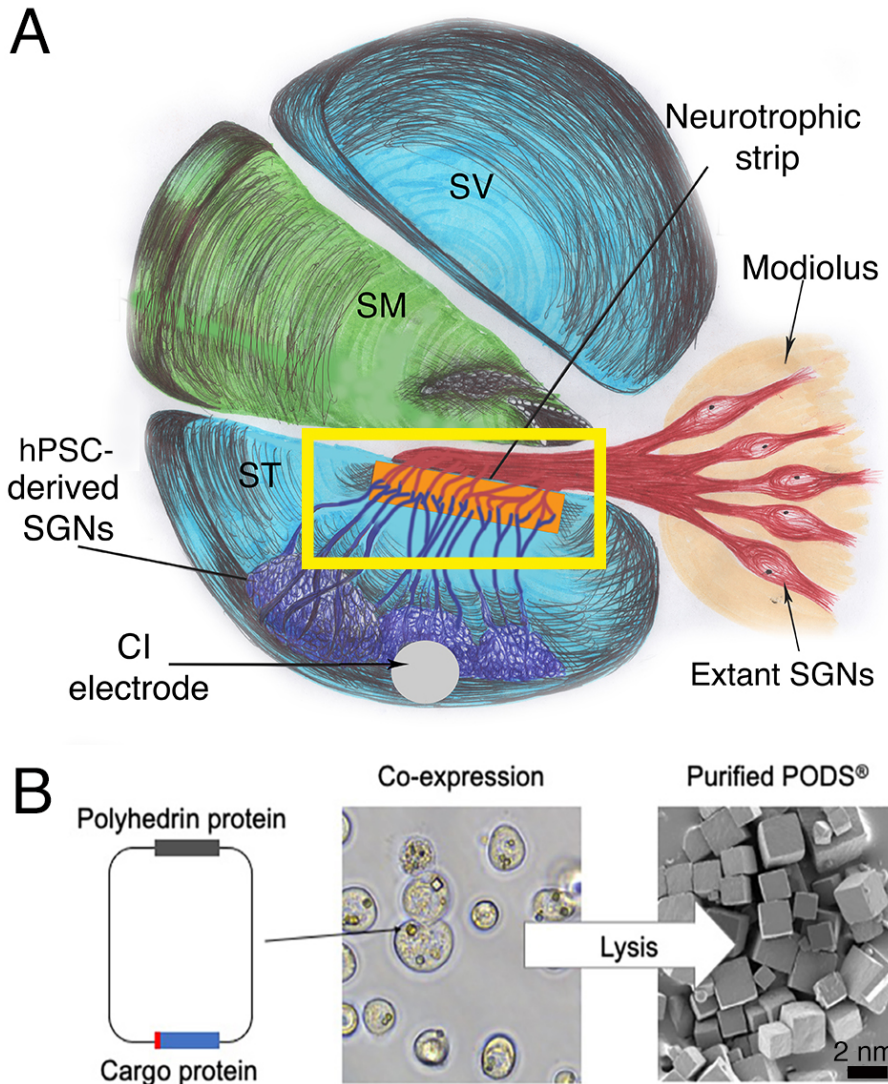


Figure 1: (A): A next-generation bioactive CI and a neurotrophic strip. The neural network in this scheme consists of a CI electrode, transplanted stem cell-derived SGNs, the neurotrophic strip, and extant/endogenous SGNs (red). Note that neuronal connection is largely absent with hair cells (not shown). (B): Polyhedrin Delivery System (PODS)®. PODS® crystals are cubic protein co-crystals produced by Sf9 cells (a clonal isolate of *Spodoptera frugiperda* Sf21 cells [IPLB-Sf21-AE], in which the polyhedrin protein and a second protein are co-expressed). This second protein is termed as the active, or cargo protein (Figure 1B, left). Inside the Sf9 cells, polyhedrin proteins self-assemble into cubic crystals (Figure 1B, center) while the active protein, tagged with a short peptide sequence, binds to the growing polyhedrin crystal. The crystals are extracted and purified by simple cell lysis and washes to remove cell debris (Scanning electron micrograph, Figure 1B, right).

62 that PODS<sup>®</sup>-human neurotrophin system could stably provide and maintain  
63 an adequate neurotrophin gradient to hPSC-derived ONPs, facilitating otic neu-  
64 ronal differentiation and directional neurite outgrowth. To test this hypothesis,  
65 we first devised a finite element model (FEM) to simulate the *in vitro* neu-  
66 rotrophin gradient generated by PODS<sup>®</sup>. In this study, we focus on the role of  
67 BDNF—the most studied of the neurotrophins in the inner ear, and the most  
68 vital for the functional recovery of damaged SGNs [20]. For biological validation  
69 and demonstration we used a multi-chamber microfluidic device, which mimics  
70 the *in vivo* micro-environment of the inner ear more so than conventional lab-  
71 oratory plates in terms of volume and concentrations of endogenous/exogenous  
72 factors [21].

73 **2. Materials and Methods**

74 *2.1. Polyhedrin delivery system*

75 The Polyhedrin Delivery System (PODS<sup>®</sup>-human BDNF [rhBDNF]) (Cell  
76 Guidance Systems, Cambridge, United Kingdom) was used as a self sustaining  
77 source of rhBDNF. PODS<sup>®</sup>-rhBDNF utilizes the polyhedrin protein formed  
78 by *Bombyx mori*, an insect from the moth family *Bombycidae*. A cargo pro-  
79 tein (i.e., rhBDNF) is co-expressed within the polyhedrin crystal and is slowly  
80 released with degradation of the PODS<sup>®</sup> crystals by cell-secreted proteases  
81 (Figure 1B)[9, 18, 22].

82 *2.2. Human pluripotent stem cell culture using dual-compartment microfluidic  
83 device*

84 Human embryonic stem cells (hESCs: H7 and H9, passages number 25–35)  
85 and were obtained from WiCell Research Institute (Madison, Wisconsin, USA).  
86 Human induced pluripotent stem cells (hiPSCs: TC-1133HKK, passage num-  
87 ber 22–35) were generated from human CD34+ cord blood cells using the four  
88 Yamanaka factors at Lonza (Walkersville, Maryland [MD], USA). The hiPSC  
89 cell line (TC-1133HKK) was kindly provided by Healios K.K. (Tokyo, Japan).

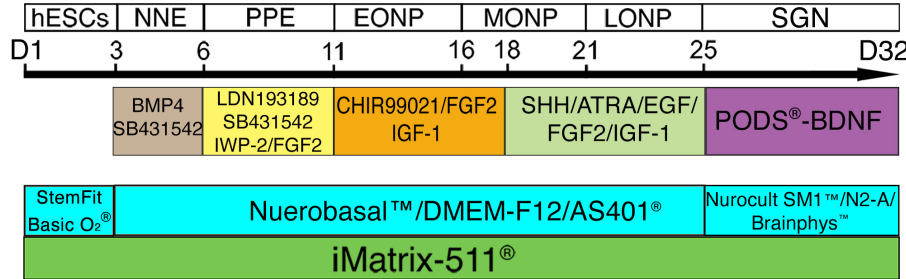


Figure 2: Overview of otic neuronal differentiation protocol for hPSCs. Please see detail in [8, 9, 23, 24] and the Supplemental Data. Each developmental stage is shown at the top, with key treatments shown below. NNE: nonneuronal ectoderm; PPE: preplacodal ectoderm; EONP: early-stage otic neuronal progenitor; MONP: mid-stage otic neuronal progenitor; LONP: late-stage otic neuronal progenitor; BMP4: bone morphogenetic protein 4; SHH: Sonic hedgehog; ATRA: all-trans retinoic acid; EGF: epidermal growth factor; IGF-1: insulin-like growth factor-1; FGF2: fibroblast growth factor 2; N2B27-CDM: chemically defined medium containing N2 and B27 supplements.

90 hPSC-derived ONPs were derived based on our previously established protocol  
 91 (Supplemental Data) [8, 9, 23, 24]. A step-wise series of ligands and growth  
 92 factors was added to a neuronal induction medium to promote hPSC differen-  
 93 tiation toward the late-stage ONP lineage—mitotic progenitor population that  
 94 generates the SGNs. (Figure 2).

95 Microfluidic devices provide a platform for specifically evaluating axonal re-  
 96 generation [25]. Here, multi-chamber microfluidic devices, Xona™ Microfluidics  
 97 XC150 and XC450 (Xona™ Microfluidics, Research Triangle Park, North Car-  
 98 olina, USA), were used for computational calculation and biological validation  
 99 (Figure 3A–B). The Xona™ device allows for neurites to grow toward growth  
 100 factors in the opposite chamber while limiting migration of derived ONP cell  
 101 bodies due to specific dimensions of the device. Additionally, the microchannel  
 102 array between the two chambers mimics the porous bony separation between  
 103 the modiolus (where extant SGNs are localized) and the scala tympani (where  
 104 the biohybrid CI will be implanted). Thus the diffusion profile of the released  
 105 rhBDNF *in vitro* more accurately predicts that of the *in vivo*.

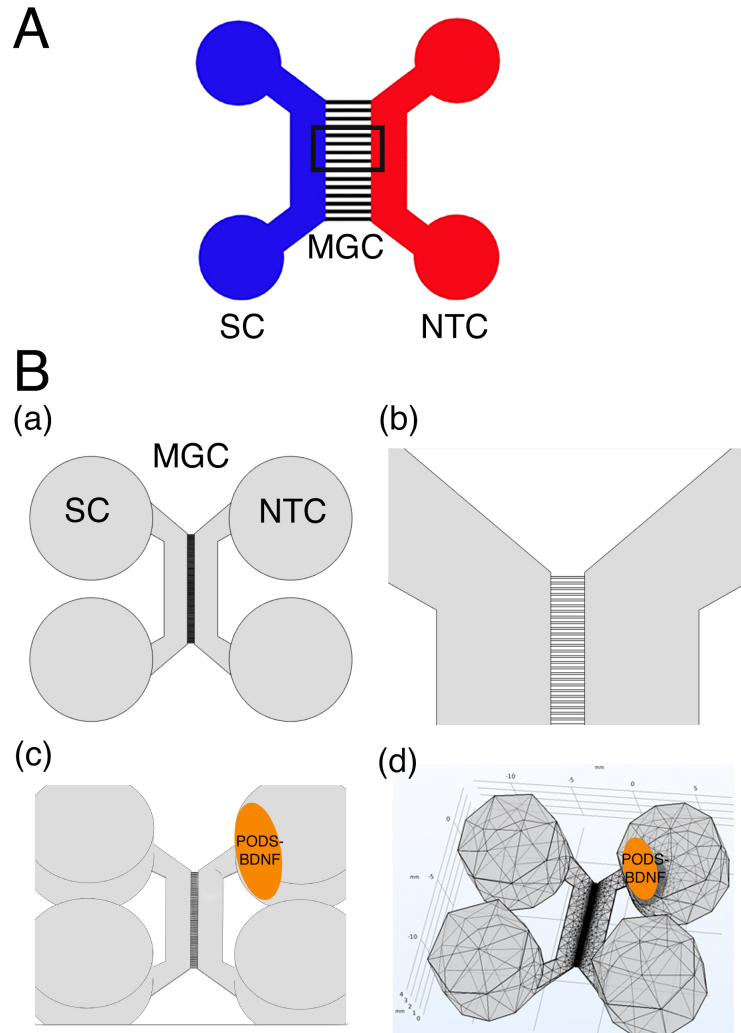


Figure 3: (A): Schematic specification of a Xona™ Microfluidics XC 450. Two main channels (somal compartment (SC) and neurotrophin compartment (NTC)) on either side are connected by a micro-groove channel (MGC) spanning  $450 \mu\text{m}$  with a width of  $10 \mu\text{m}$  (black square). The somal compartment contains hPSC-derived late-stage ONPs (shown in black), while the neurotrophin compartment contains the secreted factors (i.e., BDNF) that are released from PODS®-rhBDNF crystals. (B):(a) Xona™ Microfluidics XC450 device geometry, created at a 1:1 scale with Autodesk Inventor®, in which the diffusion profile of the released BDNF was modeled and tested. (b) Detail of the microchannels joining the two compartments of the Xona™ Microfluidics XC450. (c) Xona™ Microfluidics XC450 device showing the optimized area and geometry to localize PODS® containing rhBDNF (yellow ellipsoid area). (d): Mesh geometry of the Xona™ XC450 generated with Autodesk Inventor, depicting the localized volume of PODS®-rhBDNF ( $1 \mu\text{L}$ ) as an ellipsoid disk.

106 The devices were washed and coated with poly-L-ornithine (PLO, 20  $\mu$ g/mL  
107 in H<sub>2</sub>O, Sigma-Aldrich, St. Louis, Missouri [MO], USA) and recombinant  
108 laminin-511 (iMatrix-511, 0.5 mg/mL, Nacalai USA, San Diego, California [CA],  
109 USA) according to the manufacturer-outlined protocol. Next, approximately  
110 1.75 x 10<sup>5</sup> cells (in 20  $\mu$ L of media) were added through the top and bottom left  
111 wells to the somal compartment (i.e., the total amount of 3.5 x 10<sup>5</sup> hPSC-derived  
112 ONPs were added).

113 PODS®-rhBDNF were placed in the top right well of the neurotrophin com-  
114 partment (Figure 3A–B) to generate a BDNF concentration gradient to promote  
115 directional neurite growth. hPSC-derived ONPs were cultured for 7 days in the  
116 Xona™ device to induce otic neuronal differentiation. Note that due to our  
117 use of the microfluidic device, high-density cell cultures were induced to facil-  
118 itate molecular studies as well as the generation of a more biologically relevant  
119 neuronal phenotype (i.e., otic lineage) [25]. Media was topped off daily after  
120 imaging (from 20–40  $\mu$ L per well).

121 *2.3. Three-dimensional finite element model*

122 We used finite element analysis (FEA) to simulate the BDNF concentration  
123 gradient in a multi-chamber microfluidic device during release and subsequent  
124 degradation. FEA is a computational numerical technique, which approximates  
125 mathematical solutions to partial differential equations (PDEs) that appropri-  
126 ately simulate complex real-world problems. In this study, the finite element  
127 model allowed us to predict the concentration gradient with respect to time in  
128 the multi-chamber microfluidic device, depending on the number of PODS®-  
129 rhBDNF introduced into the system. To solve the finite element model, we used  
130 COMSOL® Multiphysics (version 5.6 [released on November 11, 2020], COM-  
131 SOL, Inc., Burlington, Massachusetts [MA], USA), which is a finite element  
132 method solution tool for engineering and scientific research computations. We  
133 used sustained-release kinetics for PODS®-rhBDNF determined from an ELISA  
134 study (see next subsection) as well as data from a previous study from our group  
135 [9]. Device geometry was generated at a 1:1 scale using Autodesk® Inventor

136 2019.0.2 (Autodesk, Mill Valley, CA, USA) (Figure 3B). The computational  
137 analysis was implemented on a high-performance desktop computer platform  
138 equipped with a CPU (AMD Ryzen Threadripper 3990X 64-Core, 128-Thread  
139 @ 4.3 GHz) with 64 GB RAM, and two GPU cards (NVIDIA GeForce RTX  
140 3080Ti,12GB 384-bit GFF6X Graphics card).

141 *2.4. Enzyme-linked immunosorbent assay for brain-derived neurotrophic factor*

142 In order to determine the release and degradation kinetics of PODS®-  
143 rhBDNF, an experiment measuring concentrations at sequential time points was  
144 performed. To measure the concentration of rhBDNF secreted from PODS®-  
145 rhBDNF crystals, the culture media from both a control and an experimental  
146 condition were collected at each time point and immediately stored at -80°C  
147 before running an enzyme-linked immunosorbent assay (ELISA) after the final  
148 collection. The same method was applied to measure the degradation kinetics  
149 of rhBDNF protein with a carrier protein (Bovine Serum Albumin [BSA])  
150 (#248-BDB-050, R&D Systems, Minneapolis, Minnesota, USA). Experimen-  
151 tal conditions were culture media enriched with 10% fetal bovine serum (FBS)  
152 (Thermo Fisher Scientific, Waltham, MA, USA). All samples were quantified  
153 with a BDNF ELISA kit (# BGK23560; PeproTech, Rocky Hill, New Jersey,  
154 USA), and the results were analyzed with a Synergy HTX Multi-Mode Reader  
155 (BioTek, Winooski, Vermont, USA) at a 450 nm wavelength, as instructed by  
156 the manufacturer. Release and degradation kinetics were then calculated using  
157 MATLAB Curve Fitting Toolbox (MathWorks, Natick, CA, USA).

158 *2.5. Sodium dodecyl sulphate-polyacrylamide gel electrophoresis*

159 Sodium dodecyl-sulfate polyacrylamide gel electrophoresis (SDS-PAGE) is  
160 commonly used as a method to separate proteins with molecular masses be-  
161 tween 5 and 250 kDa [26], a range of which is suitable for detecting human  
162 BDNF protein (molecular weight [MW]: 14kDa [27]) and polyhedrin (MW: ~29  
163 kDa [22]). In this study, SDS-PAGE was used to assess the molar ratio of  
164 BDNF to polyhedrin in each sample. Briefly, each protein sample was diluted

165 in deionized water and mixed with 6x Laemmli sample buffer (Bio-Rad Labora-  
166 tories, Inc., Des Plaines, Illinois [IL], USA) containing 2-mercaptoethanol and  
167 heated at 100°C for 5 to 20 minutes. Samples were then loaded into precast  
168 Mini-PROTEAN TGX 4-15% polyacrylamide mini-gels (Bio-Rad Laboratories,  
169 Inc., Des Plaines, IL, USA). Then, 5 mL of Precision Plus Protein Kaleido-  
170 scope Prestained Protein Standards (Bio-Rad Laboratories, Inc., Des Plaines,  
171 IL, USA) were loaded in each gel run. Electrophoresis was performed at room  
172 temperature for approximately 90 minutes using a constant voltage (100V) in  
173 1x solution of Tris-Glycine-SDS electrophoresis buffer (Bio-Rad Laboratories,  
174 Inc., Des Plaines, IL, USA) until the dye front reached the end of the 60 mm  
175 gel. After electrophoresis, the mini-gels were rinsed with deionized water 3  
176 times for 5 minutes and were subsequently incubated in SimplyBlue™ SafeStain  
177 (ThermoFisher Scientific, Waltham, MA, USA) for one hour at room temper-  
178 ature with gently agitation. Images obtained from gels were analyzed using  
179 ImageJ 1.53g (December 4, 2020, the National Institutes of Health, Bethesda,  
180 MD, USA [28]). The calculated molar ratio was applied to the COMSOL®  
181 Multiphysics model to accurately predict the amount of rhBDNF released from  
182 PODS®-rhBDNF. SDS-PAGE was performed according to the manufacturer's  
183 technical guide (Bio-Rad Laboratories, Inc., Des Plaines, IL, USA).

184 *2.6. Western Blot*

185 The identity of the BDNF protein detected by SDS PAGE was verified by  
186 western blot (Bio-Rad Laboratories, Inc., Des Plaines, IL, USA). Briefly, the  
187 polyvinylidene difluoride (PVDF) membrane was prepared in methanol for 30  
188 seconds before soaking in 1x Tris-Glycine-Methanol transfer buffer for 10 min-  
189 utes. Wet transfer was performed at 4°C for approximately 60 minutes using a  
190 constant voltage (100V) in 1X solution of Tris-Glycine-Methanol transfer buffer.  
191 After transfer, the membrane was briefly rinsed with 1X Tris-buffered saline  
192 Tween-20 (TBST) and was subsequently blocked in 5% BSA in TBST for 24  
193 hours at 4°C with gentle agitation. The membrane was then rinsed with 1x  
194 TBST before incubating in BDNF polyclonal antibody (ThermoFisher Scien-

tific, Waltham, MA, USA) diluted to 1:1500 in 1% BSA in TBST for 24 hours at 4°C with gentle agitation. Following incubation, the membrane was rinsed in 1x TBST 5 times for 5 minutes to remove unbound primary antibody. Then, the membrane was incubated in Goat anti-Rabbit IgG (H+L) horseradish peroxidase (HRP) conjugated secondary antibody (ThermoFisher Scientific, Waltham, MA, USA) diluted to 1:5000 in 1% BSA in TBST for one hour at room temperature with gentle agitation. Following incubation, the membrane was rinsed in 1x TBST 5 times for 5 minutes to remove unbound secondary antibody. For sensitive detection, the membrane was treated with Pierce™ ECL Western Blotting Substrate (ThermoFisher Scientific, Waltham, MA, USA), and visualized using an Azure 600 Digital Imager (Azure Biosystems, Dublin, CA, USA). Electrophoresis buffer for sample condition and run condition was summarized in Supplementary Table S1.

*2.7. Immunocytochemistry and image acquisition*

Glass coverslips (Corning Inc., Corning, New York, USA) were coated with poly-d-lysine (PDL) (#A3890401, ThermoFisher Scientific, Waltham, MA, USA) and poly-ornithine (PLO) (# A-004-C, MilliporeSigma, St. Louis, MO, USA) affixed to a somal compartment as per the manufacturer's instructions. A total of 100,000 dissociated hPSC-derived ONPs were plated onto a somal compartment of the device. On Day 7, 4% (w/v) paraformaldehyde (PFA) (ThermoFisher Scientific, Waltham, MA, USA) was added to the compartments for 20 minutes to fix the cells. ICC was used to stain for GATA3, PAX8, and beta-III tubulin. These three proteins have shown to appropriately characterize ONPs in our previous studies [8, 9, 24]. Following PBS wash, cultures were blocked with 5% BSA at room temperature for 1 hour. Cultures were then incubated overnight at 4°C on a shaker plate in primary antibody solution using Rabbit anti-Beta-III-Tubulin (1:100, Abcam, Cambridge, MA, USA), Goat anti-PAX8 (1:500, Abcam, Cambridge, MA, USA), and Mouse anti-GATA3 (1:500, R&D Systems, Minneapolis, MN, USA). Following PBS washes, cultures were incubated at room temperature for 90 minutes on a shaker plate in sec-

225      ondary antibody solution composed of Alexafluor647 anti-Rabbit (1:1000, Ther-  
226      moFisher Scientific, St. Louis, MO, USA), Alexafluor488 anti-Goat (1:1000,  
227      ThermoFisher Scientific, St. Louis, MO, USA), and Alexafluor594 anti-Mouse  
228      (1:1000, ThermoFisher Scientific, St. Louis, MO, USA) in 1% BSA. Following  
229      PBS -/- washes, cultures were incubated with DAPI for 20 minutes (300 nM,  
230      ThermoFisher Scientific, St. Louis, MO, USA). Secondary antibody controls  
231      were performed each time multiple primary antibodies were used [29]. Label-  
232      ing controls (detection controls) were performed for a sample from each batch  
233      of hPSC culture [29]. See Supplementary Figure S1 for exemplary figures for  
234      these control conditions. Results were imaged using a Nikon Ti2 Widefield  
235      Laser Microscope System (Nikon, Tokyo, Japan). Phase-contrast images were  
236      captured on a Nikon Eclipse TE2000-U inverted microscope (Nikon, Tokyo,  
237      Japan). All fluorescence images were acquired on a Zeiss LSM 510 META laser-  
238      scanning confocal microscope (Carl Zeiss, Oberkochen, Germany), a Nikon Ti2  
239      laser laser-scanning confocal microscope (Nikon, Tokyo, Japan), or a Leica SP5  
240      laser-scanning confocal microscope (Leica, Welzlar, Germany). Observers were  
241      blinded to the conditions during imaging and tracing. In general, the images  
242      were processed with a Image J ver. 1.53j or Matlab R2020b. Further detail on  
243      image acquisition and quantification of fluorescent-positive cells can be found  
244      in the Supplemental Data.

245      *2.8. Preferred cell orientation analysis*

246      Collective cell migration, where cells organized in a tightly connected fashion  
247      migrate as cohesive structures, is a critical biological process to highlight the  
248      neurotrophin diffusion gradient profile [30]. To evaluate this process, time-lapse  
249      acquisition of images of the Xona™ device was performed using an inverted mi-  
250      croscope (Nikon Eclipse TS100, Tokyo, Japan) at Day 1, 3, 5, and 7. Due to the  
251      high cell density required for hPSC-ONPs to survive in the somal compartment  
252      of the Xona™ device, images were not amenable to manual analysis in most of  
253      the cases. To circumvent this problem, we performed a series of image pre-  
254      processings that are mainly based on modified binarization-based extraction of

aliment score methods with some modifications [31]. We used MATLAB Image Processing Toolbox R2020b (version 9.9.0.1495850, September 30th, 2020, Mathworks, Natick, MA) for analysis. Please see Supplementary Figure S2 for further detail. The analysis of directional data in general represents a particular challenge: there is no reason to designate any particular point on the circle as zero, as it is somewhat arbitrary depending on where one sets a coordinate [32, 33]. In this study, we used polar coordinates to determine the directionality of preferred cell orientation. For this analysis, we again used MATLAB Image Processing Toolbox R2020b. See detailed discussion on how we determined the preferred cell orientation in Supplementary Figure S3.

*2.9. Neurite alignment vector assay, neurite growth assay and cell migration assay*

The microfluidic device allowed us to culture hPSC-derived ONPs in a polarized manner and to directly isolate/analyze neurites. To evaluate the neurite projection into the neurotrophin compartment by derived otic neurons cultured in the somal compartment, we performed a neurite alignment vector assay. We also evaluated the length of neurites that grew from hPSC-derived ONPs. For these purposes, hPSC-derived ONPs were cultured in a Xona™ XC450 for seven days and then immunostained with *beta*-III tubulin and DAPI. We used two ImageJ plug-in toolkits, NeuriteTracer and NeuronJ, to assess neurite alignment and neurite growth [34, 35]. Due to the bipolar nature of hPSC-derived ONPs/SGNs, we measured the two longest neurites from the cells [24, 36]. Please see Supplementary Figure S4 for detailed description of this analysis. We used hPSC-derived ONPs cultured with 800,000 PODS®-rhBDNF as a positive control. The number 800,000 was chosen based on our FEM in that there was no neurotrophin gradient in a somal compartment. As a negative control, we used 20 ng/mL of recombinant human BDNF. To evaluate cell migration across a microgroove channel, we performed cell migration analysis. We manually counted the number of ONPs that migrated from the somal compartment into the microchannels, as well as the neurotrophin compartment.

285     *2.10. Statistical analysis*

286     When appropriate, and as indicated in each figure, statistical analysis was  
287     performed. Experimental values are typically expressed as mean and standard  
288     error (SE). The majority of the statistical analyses were performed with Python  
289     3.9.6. (Python Software Foundation, Wilmington, Delaware, USA). The follow-  
290     ing libraries were used for the statistical analysis: Scipy, Numpy, Matplotlib,  
291     and Seaborn [37, 38, 39]. Normal distributions were assumed unless mentioned  
292     otherwise. *P* values smaller than 0.05 were considered statistically significant.  
293     For circular statistics, we derived the sample mean vector and its polar coor-  
294     dinate. Mean and confidence intervals were calculated. We chose confidence  
295     coefficient, *Q*, e.g. *Q* = 0.95. To analyze the axial nature of data, especially to  
296     compute the mean vector angle, we doubled each angle and reduced the mul-  
297     tiples modulo 360°. Please see detailed discussion in Supplementary Figure S3  
298     and S5. The Rayleigh test of uniformity and V-test were performed to deter-  
299     mine whether the samples differ significantly from randomness (i.e., where there  
300     is statistical evidence of directionality). One-sample test for the mean angle was  
301     performed to test whether the population mean angle is statistically different  
302     from the given angle. In all of our circular statistics, von Mises distribution was  
303     assumed and also verified. Circular statistics were performed using CircStat: A  
304     MATLAB Toolbox [33, 40]. Please see detailed description of circular statistics  
305     in Supplementary Figure S3 and S5. Experiments were done in three biological  
306     replicates unless otherwise specified in Figure captions.

307     **3. Results**

308     The appropriate number of PODS®-rhBDNF crystals to induce an effective  
309     neurotrophin gradient for otic neuronal differentiation and neurite outgrowth  
310     was calculated using a three-dimensional FEA that predicts the concentration  
311     profile of BDNF formed through the gradual release and diffusion of BDNF  
312     from PODS®-rhBDNF. We first empirically tested two available microchannel  
313     lengths—(i.e., Xona™-XC150 [150 μm] and Xona™-XC450 [450 μm]). This was

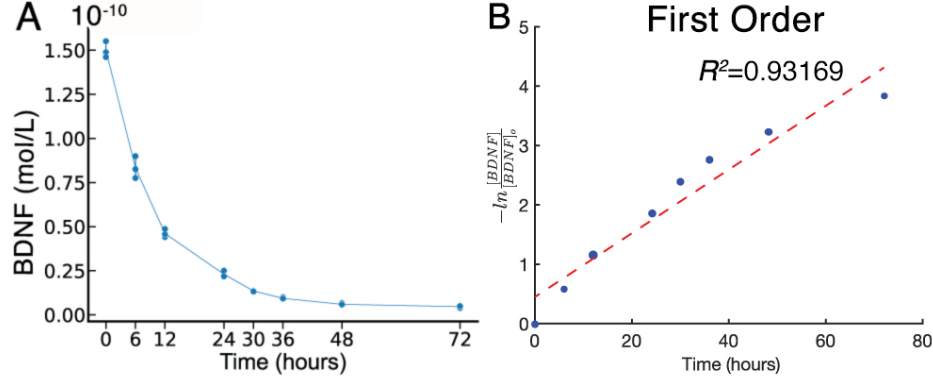


Figure 4: Chemical kinetics of Brain Derived Neurotrophic Factor (BDNF). (A): Concentration of rhBDNF in solution over 72 hours after initial application. (B):  $\frac{1}{[BDNF]}$  data fit to first order curve. Please see other curve fit data in Supplemental Figure 1. Red line: fitted line, blue dots: individual data point.  $k_2$  is defined as slope of fitted curve.

314 done initially because mass (i.e., BDNF) transport from the neurotrophin com-  
 315 partment through the micro-groove channels into the somal compartment is an  
 316 important factor in generating the concentration gradient *via* diffusion mixing.  
 317 We determined that the Xona™ Microfluidics XC450 was more appropriate for  
 318 this study as the XC-150's micro-groove channels were not long enough to gener-  
 319 ate the appropriate concentration gradient throughout the somal compartment.  
 320 This feature is relevant to human inner ear because the micro-groove channels in  
 321 the Xona device simulates the presence of the osseous spiral lamina and modi-  
 322 olus between the scala tympani and SGNs [41, 42]. Following device selection,  
 323 we generated a three-dimensional geometry mesh of the Xona™ Microfluidics  
 324 XC450 for the FEA (Figure 3B(d)). Please also see Supplementary Figure S6  
 325 for detailed measurements of the mesh.

We then quantified the chemical kinetics of the degradation of PODS®-rhBDNF followed by the release and eventual degradation of the rhBDNF by ELISA testing (Figure 4) to establish the parameters for the FEA. Here, two consecutive chemical reactions occur: 1) the release of rhBDNF through degra-  
 dation of PODS® crystals, and 2) the degradation of rhBDNF toward the degra-

dation product (Equation (1)).



326 where  $DP$  is the degradation product of the released rhBDNF, and  $k_1$  and  $k_2$   
 327 are the rate constants ( $\frac{1}{hour}$ ) for their respective reactions.

328 Degradation kinetics for rhBDNF was collected while monitoring rhBDNF  
 329 concentration after introducing a predefined amount into a single well of solu-  
 330 tion. The data obtained throughout the first 72 hours indicate an exponential  
 331 decay, suggesting first order kinetics (Figure 4). To confirm this notion, we  
 332 performed a linear and nonlinear least square analysis of the kinetic data with  
 333 the MATLAB Curve Fitting Toolbox. We found that the corresponding  $R^2$  was  
 334 0.93169 for the first order curve-fit, confirming that the degradation kinetics  
 335 was indeed first order. The value for  $k_2$  ( $0.0679 (\frac{1}{hour})$ ) was derived from  
 336 the curve-fit (See further detail in Supplementary Figure S7). Furthermore,  
 337 data for the complete chemical reaction were collected by monitoring rhBDNF  
 338 concentration over time after placing a predefined amount of PODS<sup>®</sup>-rhBDNF  
 339 into a single well of solution. The data collected appeared to fit the curve for  
 340 Equation 2, which describes the concentration of the intermediate product of  
 341 two consecutive first order reactions:

$$C_{rhBDNF} = C_{PODS} \cdot k_1 \cdot \left( \frac{e^{-k_1 \cdot t}}{k_2 - k_1} + \frac{e^{-k_2 \cdot t}}{k_1 - k_2} \right) \quad (2)$$

342 where  $C_{rhBDNF}$  is the concentration of rhBDNF and  $C_{PODS}$  is the concentra-  
 343 tion of PODS<sup>®</sup> [43].

344 We successfully fit the data to this curve and empirically approximated  $k_1$   
 345 ( $0.00686 (\frac{1}{hour})$ ), allowed by our calculation of  $k_2$  (See further detail in Supple-  
 346 mentary Figure S7). Using these rate constants, the resulting chemical gradient  
 347 over time after PODS<sup>®</sup>-rhBDNF placement can be solved for any geometry  
 348 by applying Fick's second Law of diffusion and the appropriate boundary and  
 349 initial conditions:

$$\frac{\partial C}{\partial t} = \nabla \cdot (\nabla C \cdot D) - k_2 \cdot C \quad (3)$$

Boundary conditions:

$$\delta C \Big|_{walls} = 0 \quad (4)$$

350 and

$$\delta C \Big|_{PODS} = k_1 \cdot PODS_0 \cdot e^{-k_1 \cdot t} \quad (5)$$

Initial conditions:

$$C \Big|_{t=0} = 0 \quad (6)$$

351 where  $C$  is the concentration of rhBDNF,  $D$  is diffusivity of rhBDNF (6.76  
352  $\frac{mm^2}{day}$  [44]),  $-k_2 \cdot C$  is the sink term corresponding to the degradation and cell-  
353 utilization of the rhBDNF.  $PODS_0$  is the initial concentration of the cargo  
354 protein (i.e., BDNF) within the PODS® crystals. The first boundary condition  
355 (Equation 4) shows that the concentrations of rhBDNF at the walls of the  
356 microfluidic device are fixed at 0. The second boundary condition (Equation 5)  
357 represents the exponential nature of decay of the PODS®. Note that both of  
358 them are Neumann boundary conditions.

359 As mentioned, we used the first-order fitted data from our ELISA experi-  
360 ment and then determined the values of the  $k_{1,2}$  coefficients, which were then  
361 applied to the diffusion equation. The finite element model was then computed  
362 for different PODS®-rhBDNF concentrations and time intervals to optimize  
363 the rhBDNF concentration gradient for hPSC-derived ONP differentiation into  
364 SGNs and directed neurite extension. Figure 5 shows FEA-computed rhBDNF  
365 concentration gradient for 20,000 PODS®-rhBDNF from Day 1–7. Note that  
366 the BDNF concentrations were greater on D2–5 to promote neuronal differentia-  
367 tion and neurite outgrowth observed on D7 (Figure 5B). Computed diffusion flux  
368 was uniform throughout D1–7 (Figure 5C). Also note that highest concentra-  
369 tion of rhBDNF released from PODS®-crystals was greater than 50 pg/mL, the  
370 concentration sufficient for otic neuronal differentiation and neurite outgrowth  
371 of hPSC-derived ONP 3D spheroids from our previously published data [9].

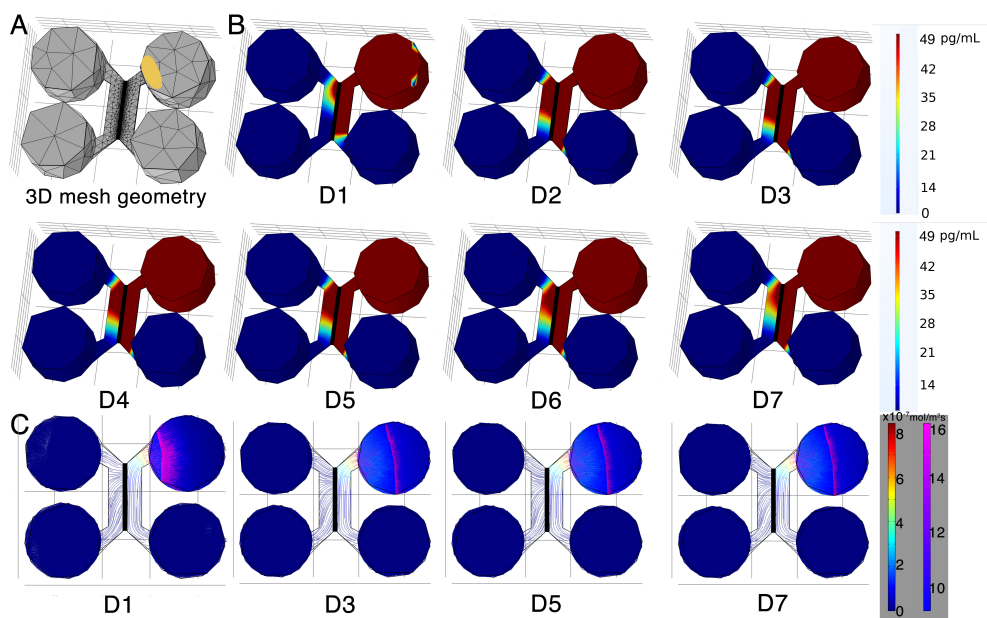


Figure 5: (A): 3D mesh geometry of a Xona™ XC450 created with Autodesk Inventor. An ellipse-shaped PODS®-rhBDNF disc is shown in yellow. (B): Human BDNF concentration gradient for 20,000 PODS®-rhBDNF from D1–D7. Note that the model does not account for media changes during the culture period. The corresponding color map is shown a range from 0 ng/mL to 49 ng/mL. (C): Diffusion flux ( $mol/m^2 s$ ) was computed using COMSOL Chemical Engineering module on D1, D3, D5, and D7.

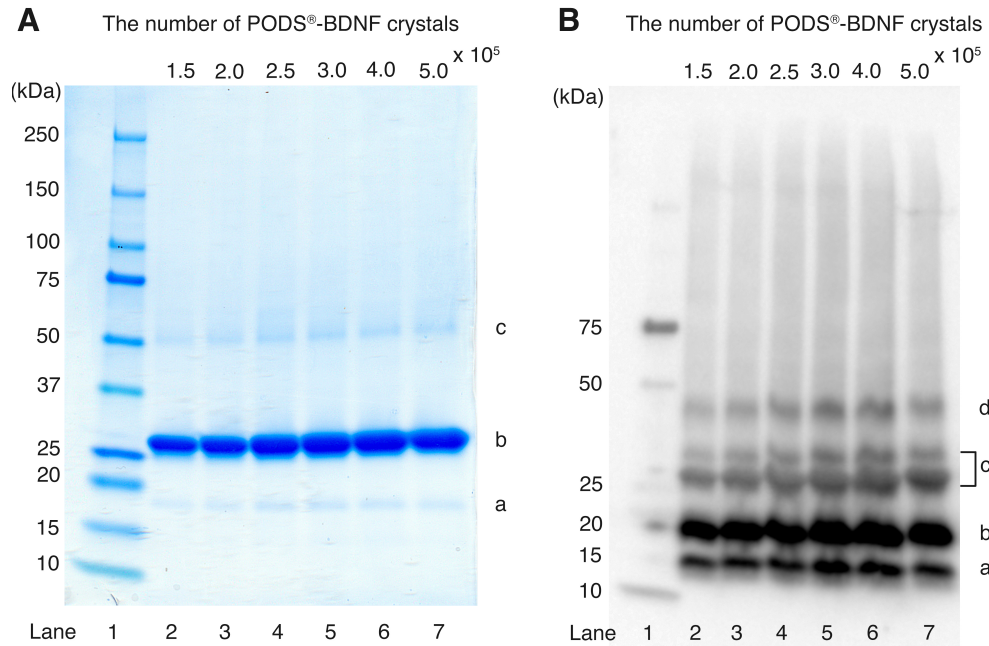


Figure 6: (A): SDS-PAGE analysis of PODS<sup>®</sup>-rhBDNF. Samples containing six quantities of PODS<sup>®</sup>-rhBDNF crystals were run on precast 4-15% polyacrylamide mini-gels and stained with Coomassie G-250 solution for visualization. Protein bands appear at approximately 18.8 (a), 28.0 (b), and 46.8 kDa (c). Lane 1: molecular weight marker. Lanes 2-7: samples containing

372 For the optimization process in determining the adequate number of PODS<sup>®</sup>-  
 373 rhBDNF, we also performed FEA with 10,000 and 40,000 PODS<sup>®</sup>-rhBDNF.  
 374 Please see detailed discussion of how we determined the optimum concentration  
 375 of 20,000 PODS<sup>®</sup>-rhBDNF in Supplementary Figure S8.

376 SDS-PAGE was used to separate PODS<sup>®</sup>-rhBDNF crystals into its con-  
 377 stituent proteins to determine the molar ratio of polyhedrin to BDNF. Visu-  
 378 alization with Coomassie G-250 solution (Figure 6A) revealed three distinct  
 379 protein bands at 18.8 (a), 28.0 (b), and 46.8 (c) kDa, which correspond with  
 380 the molecular weights of H1-tagged BDNF monomer, polyhedrin, and H1-tagged  
 381 BDNF monomer attached with polyhedrin, respectively. Western blot analy-  
 382 sis was subsequently conducted to confirm the identity of the 18.8 kDa band

383 as rhBDNF. Enhanced chemiluminescence (Figure 6B) revealed four protein  
384 bands at 14.0 (a), 18.8 (b), 37.6 (c), and 46.8 (d) kDa, which correspond with  
385 the molecular weights of rhBDNF monomer, H1-tagged BDNF monomer, H1-  
386 tagged BDNF dimer, and H1-tagged BDNF monomer attached with polyhedrin.  
387 Immunoblot detection of the 18.8 kDa band further implicates its identity as  
388 rhBDNF. SDS-PAGE images were converted to 8-bit grayscale and mean cor-  
389 rected integrated pixel intensity values were calculated for protein bands located  
390 at 28.0 and 18.8 kDa; the protein band detected at 46.8 kDa was omitted from  
391 the final computation based on the notion that it contained a 1:1 ratio of poly-  
392 hedrin to BDNF. Results indicate that the molecular ratio of polyhedrin to  
393 rhBDNF is approximately 17:1.

394 To objectively compare the degree of otic neuronal differentiation in hPSC-  
395 derived ONPs, we performed quantitative analysis of PAX8 and GATA3 double-  
396 positive cells using immunocytochemistry. We chose PAX8 and GATA3 for this  
397 analysis because our previous studies indicated high expression of these protein  
398 markers in late-stage ONPs and early-stage SGNs [8, 9, 24]. Cells were stained in  
399 the somal compartment of the Xona™ device, highlighted in green in Figure 7A.  
400 Figure 7B shows the resulting image of cells in the somal compartment, and  
401 a heat-map representation of the percentage of double-positive cells is shown  
402 in Figure 7C. It should be noted here that the heatmap is sensitive to the  
403 differences in cell density across channel. This was accounted by averaging  
404 the double-positivity across three biological replicates. The heat-map indicates  
405 higher double-positivity in the upper region of the somal compartment, which  
406 is closest to the PODS®-rhBDNF disc placement (shown in a orange ellipse in  
407 Figure 7A) in the neurotrophin compartment. Double-positivity decreases in  
408 the somal compartment as distance from the PODS®-rhBDNF disk increases,  
409 supporting the presence of a BDNF neurotrophin gradient as predicted by our  
410 computational model calculation (Figure 7D).

411 We defined two hypothetical directional angles to predict the orientation of  
412 hPSC-derived ONPs and neurite growth (Figure 8). The  $n$ -dimensional Eu-  
413 clidean space, denoted by  $\mathbb{R}^n$ , is a linear vector space in that we can use polar

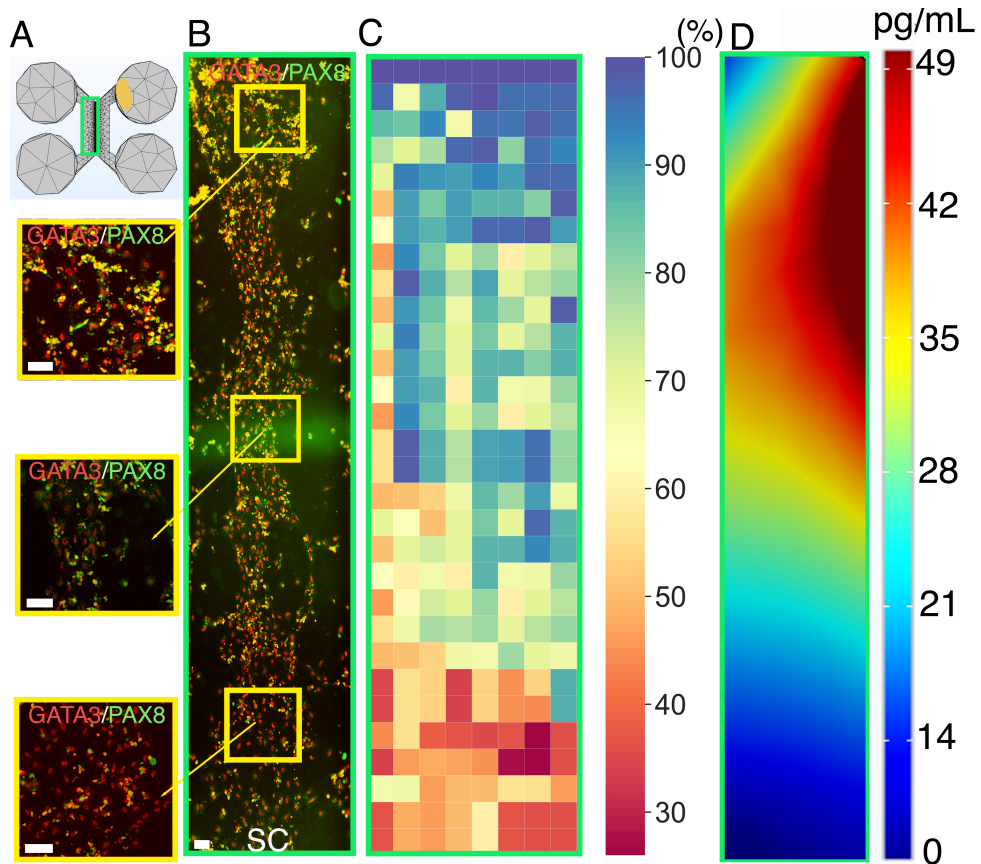


Figure 7: Human PSC-derived late-stage ONPs grown in a microfluidic device at Day 7 were stained for GATA3 (red) and PAX8 (green). (A): Geometry mesh of the microfluidic device Xona™ XC450 generated by Autodesk Inventor. The green square indicates the cell seeding location in the somal compartment of the device. An ellipse-shaped PODS®-rhBDNF disc is shown in yellow. (B): Cells were analyzed by staining with neuronal markers GATA3 (red) and PAX8 (green). Yellow highlighted regions are magnified on the left. SC: somal compartment. (C): Heat-map representation of double-positivity of hPSC-derived ONPs in the device for GATA3 and PAX8 ( $n = 3$ ). Double-positivity increases from the lower to the upper portion of the somal compartment, suggesting that the higher BDNF concentration in the upper portion of the device improves differentiation. Scale bar: 100  $\mu\text{m}$ . (D): Prediction of BDNF concentration gradient released from PODS®-rhBDNF at seven days in culture using a finite element model. The corresponding color map is shown with a range from 0–49 pg/mL.

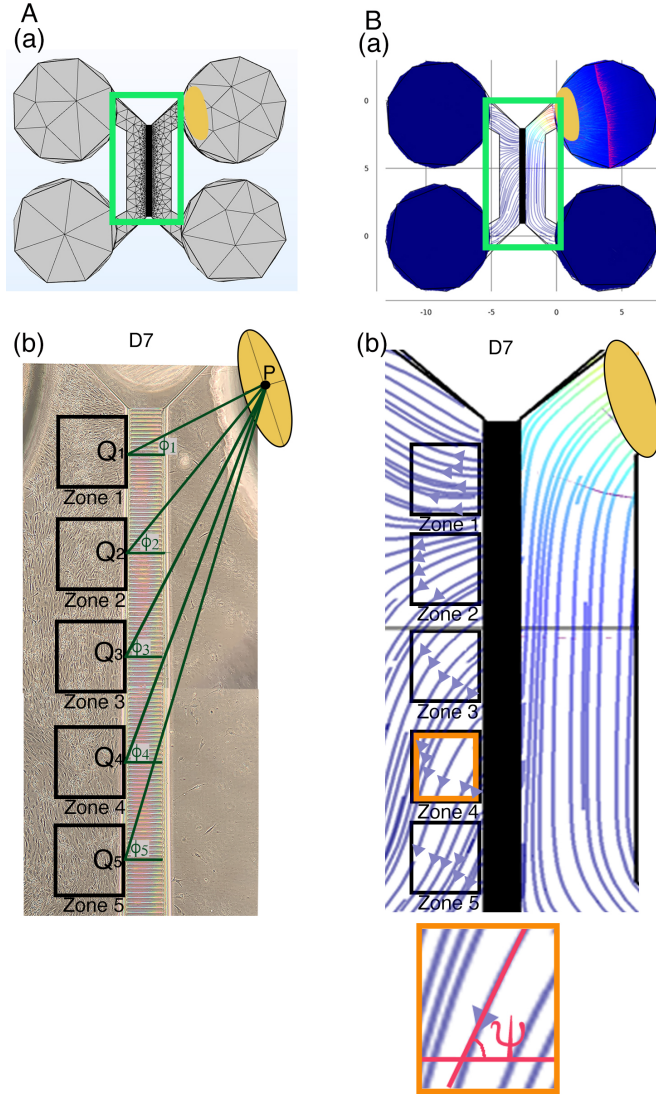


Figure 8: (A): Defining the Euclidean distance angle (EDA). (a) X-Y plane geometry mesh of a Xona™ XC450 device. Green square shows an area corresponding to a phase-contrast image below. An ellipse-shaped PODS®-rhBDNF disc is shown in yellow. (b) hPSC-derived ONPs were cultured in a Xona™ XC450 for seven days (D7). Yellow ellipse once again indicates the location of a disk contains PODS®-rhBDNF crystals (P: the center of this ellipse). In the somal compartment of the Xona™ XC450 device, we defined Zone 1–5, shown in black square. A line was drawn from the center of the PODS®-rhBDNF disk (P) to (Q<sub>1–5</sub>) (i.e., the near side to microgroove channels) of a pre-designated square (shown as a black square, zone 1–5) [i.e.,zone 1–5]. The Euclidean distance angle (EDA) for zone 1–5 was defined as  $\phi_i$ ,  $i = 1–5$ . (B): Defining diffusion flux angle (DFA). (a) Diffusion flux in a Xona™ XC450. Green squared area show a somal and neurotrophin compartment, which are magnified in (b). (b) Magnified image of diffusion flux of Zone 1–5 in a Xona™ XC450. Orange highlighted zone (zone 4) was magnified at the bottom of (b), defining a DFA ( $\psi$ ).

414 coordinates to compute the directionality of cells and neurites [45]. Here, we  
415 used  $n = 1$  and 2. For one-dimensional Euclidean space ( $n = 1$ ), we simply drew  
416 a line for the Euclidean distance—the shortest distance between two points as  
417 shown in Figure 8A(b) (dark green lines). The two points were 1) the center  
418 point of a PODS®-rhBDNF disk ( $P$ ) and 2) the mid point of the medial side  
419 (i.e., the near side to microgroove channels) of a pre-designated square  
420 (shown as a black square, zone 1–5 in Figure 8), respectively. The Euclidean  
421 distance angle (EDA),  $\phi_i$ , was defined as the angle between the horizontal line  
422 zero direction and the line  $PQ_i$  that consists of the Euclidean distance where  $i$   
423 = 1–5.

424 For two-dimensional Euclidean space ( $n = 2$ ), we utilized Fick’s first law,  
425 which dictates that the diffusion flux ( $D$ ) is proportional to the concentration  
426 gradient ( $C$ ) [46]. Based on this theorem, the direction of a flow vector can  
427 be used to represent concentration gradient for the directionality. We hypothe-  
428 sized here that cell orientation is directionally controlled by the flux vector  
429 which is driven by the concentration gradient. Figure 8B shows the flow vectors  
430 in a somal compartment at Day 7 computed by COMSOL Chemical engineering  
431 module. We averaged the 10 flow vectors in each of five zones in Figure 8 to  
432 compute diffusion flux angle (DFA),  $\psi_i$ , where  $i = 1–5$  in Figure 8. To lighten  
433 the computational intensity, we reduced a dimension from 3D to 2D to com-  
434 pute diffusion Flux. Please see justification in Supplementary Data. All of the  
435 computed EDAs and DFAs can be found in Supplementary Table 2.

436 Figure 9 shows time-series of microscopic phase-contrast photomicrographs  
437 obtained on Day 1, 3, and 7 in the five zones in a Xona™ XC450. Each preferred  
438 orientation of any given cell was computed and then plotted on a polar diagram  
439 (blue circle). Mean vector angle (MVA, shown in red line on Figure 9) and  
440 median vector angle were computed. All of the polar diagrams in Figure 9 show  
441 that preferred orientation of hPSC-derived ONPs distribute in an unimodal dis-  
442 tribution. We also confirmed that a von Mises distribution is appropriate for  
443 these sets of data (See Supplementary Figure S9). We, therefore, then tested  
444 further to see if the cells had tendency to be oriented to a certain direction.

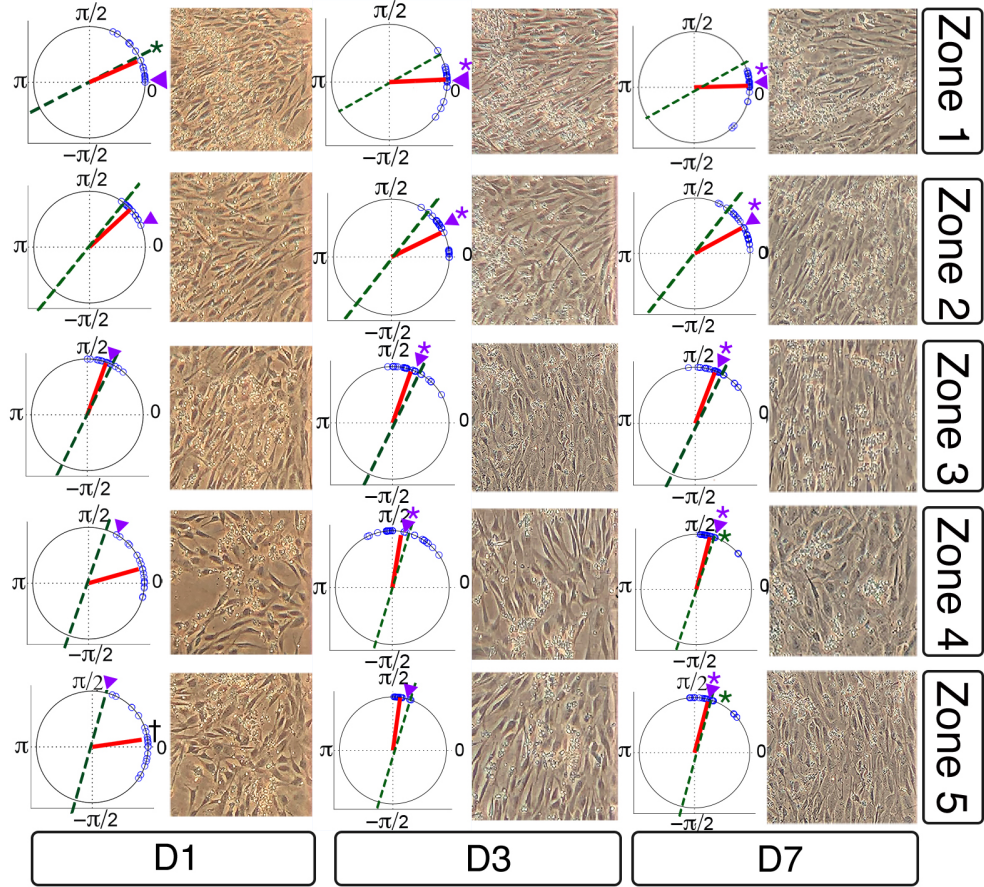


Figure 9: Preferred cell orientation analysis. Sequential phase-contrast images of a somal compartment of a Xona™ XC450 device in zone 1–5 (see Figure 8) on day 1 (D1), day 3 (D3), and day 7 (D7). A corresponding polar histogram indicates preferred orientation of hPSC-derived ONPs in an angle ( $0$ – $2\pi$  radians) in blue circles. Mean vector angle is shown in red line. Green dotted line shows Euclidean Distance Angle (EDA) and purple triangle indicates Diffusion Flow Angle (DFA). † symbol indicates that  $p$  value  $> 0.01$ . \* symbol indicates that the mean vector angle fits within the 95% confidence internal ( $\alpha < 0.05$ .)

445 To test this hypothesis, we used the Rayleigh test of uniformity to evaluate  
446 whether there is statistical evidence of circular directionality [32]. Computed  
447  $p$  values for all the 15 conditions were less than 0.05, demonstrating that all  
448 of the conditions had statistically significant directionality. To further validate  
449 whether the observed angles have a tendency to cluster around the two hypo-  
450 thetical angles (i.e., EDA and DFA), we then performed the V test. Once again,  
451  $p$  values for all 15 conditions were less than 0.05 except one (Zone 5 on Day 1),  
452 re-demonstrating that most of the conditions had statistically significant ten-  
453 dencies to cluster around the EDAs and DFAs. Finally, to investigate whether  
454 the preferred orientation of the cells were clustered around the EDAs or DFAs,  
455 we performed one sample test for the mean vector angle, which is similar to a  
456 one sample t-test on a linear scale. There was only one condition (Zone 1, day  
457 1) that was statistically significant for EDA, whereas most of the conditions on  
458 Day 3 and 7 were statistically significant for DFA. Therefore, our results here  
459 demonstrated that hPSC-derived ONPs had greater tendency to cluster around  
460 DFA than EDA. All computed statistical values are shown in Supplementary  
461 Table S2.

462 To evaluate the direction of neurites of hPSC-derived ONPs, we first de-  
463 fined EDA in Region 1-3 ( $\phi'_j$ ,  $j = 1 - 3$ ) (Figure 10A) and DFA ( $\psi'_j$ ,  $j = 1-3$ );  
464 similarly defined  $\phi_i$  and  $\psi_i$  as in Figure 8. All of the EDAs and DFAs defined  
465 here can be found in Supplementary Table S3. Polar histograms of the neurite  
466 direction angle in Region 1–3 indicated that the two longest neurites were bi-  
467 modal in nature (Figure 10B). In contrast, polar histograms of those cultured  
468 with rhBDNF (negative control) and 800,000 PODS®-BNDF (positive control)  
469 did not indicate bimodal distribution—the neurites did not show directionality  
470 (Figure 10C). The Rayleigh test of uniformity for both the positive and negative  
471 control were greater than 0.05, demonstrating that both of the conditions had  
472 no statistically significant directionality (Supplementary Table S3: highlighted  
473 in green). We also analyzed the direction of the neurites using circular statistics.  
474 To obtain more realistic mean vector angles, we doubled each angle and reduced  
475 the multiples modulo 360°. In circular statistics, the bimodal distributed data

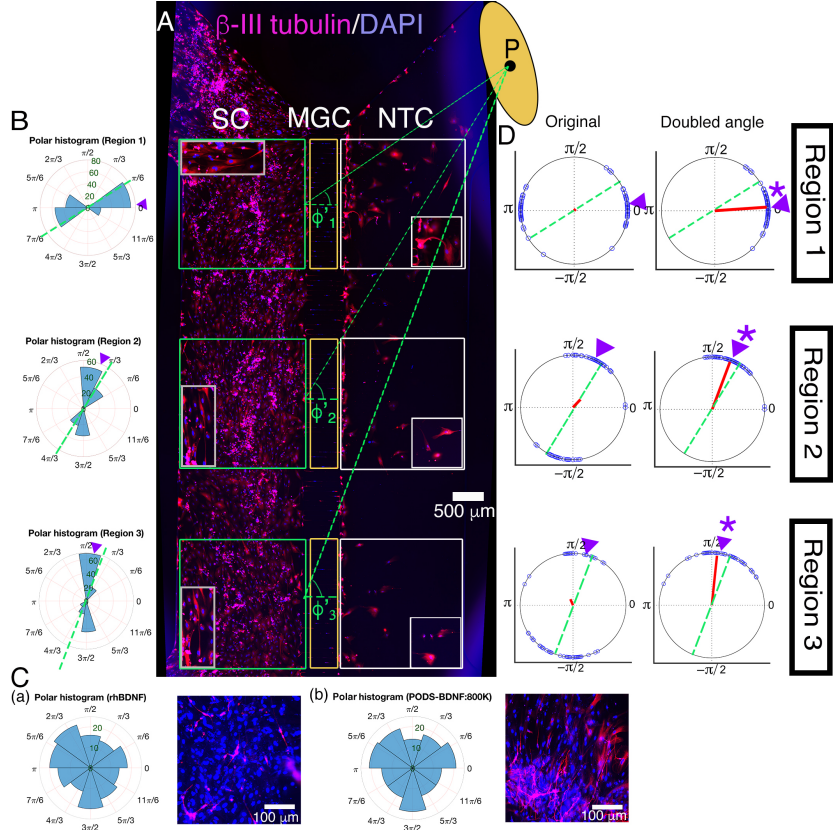


Figure 10: (A): Immunohistochemistry of hPSC-derived ONPs cultured in the Xona™ XC450 for seven days with  $\beta$ -III-Tubulin (pink fluorescence) and DAPI (blue fluorescence). A green line was drawn from the center of the BDNF disk (P) to the mid point of each of three pre-determined squares (Region 1–3) in the somal compartment to define Euclidean Distance Angle (EDA:  $\phi_i^*$ ,  $i = 1 - 3$ ). Green square: somal compartment (SC); yellow square: microgroove channels (MGC); White square: Neurotrophin compartment (NTC). High-power magnified images of the NTC and SC are shown. An ellipse-shaped PODS®-rhBDNF disc is shown in yellow. P: the center of the disk.(B): Polar histogram of neurite directional angles of hPSC-derived ONPs in the Xona™ XC450 at Day 7 (D7). The two longest neurites were measured. EDA: green dotted line. DFA: purple triangle. (C): (a) Right: Polar histogram of neurite directional angles of hPSC-derived ONPs cultured with 20 ng/mL of recombinant human BDNF for seven days. Left: Corresponding photomicrograph of immunocytochemistry with  $\beta$ -III tubulin (pink) and DAPI (blue). (b) Right: Polar histogram of neurite directional angles of hPSC-derived ONPs cultured with 800,000 of PODS®-rhBDNF for seven days. Left: Corresponding photomicrograph of immunocytochemistry with  $\beta$ -III tubulin (pink) and DAPI (blue). (D): A circular plot of neurite directional angle of hPSC-derived ONPs in Region 1–3. Once again, the two longest neurites were plotted on a unit circle. Right column: Original directional angle distribution. Left column: the method of doubling the angle applied to the original data. Each datum point is shown as a blue circle. Mean vector angle is shown as a red line. Green dotted line shows Euclidean Distance Angle (EDA) and purple triangle indicates Diffusion Flow Angle (DFA). \* symbol indicates that the mean vector angle fits within the 95% confidence internal ( $\alpha < 0.05$ .)

476 can be transformed into a unimodal data by doubling the angle [32]. The mean  
477 vector angles in Figure 10D (right column) indicates the situation where the  
478 vectors were canceled out between the two groups of angles distributed in a bi-  
479 modal fashion, resulting in inaccurate representation. A circular plot in Figure  
480 10D (right column) showed doubled angles, representing actual representation  
481 of the neurite vector angles. In all of the three regions, the Reyleigh test and V  
482 test for EDA and DFA indicated directionality (Supplementary Table S3). One  
483 sample test for the mean vector angles in Region 1–3 indicated that they were  
484 not statistically different from DFA, but all of the three mean vector angles were  
485 statistically different from EDA.

486 We also stained the devices for  $\beta$ -III tubulin to track neurite growth and  
487 extension across the micro-groove channels as well as cell migration in three  
488 selected regions (Figure 10A). The location of the PODS®-rhBDNF disk in  
489 relation to the regions of interest in Figure 11A is indicated by a yellow circle.  
490 Quantitative analyses were performed and summarized in Figure 11B. Our data  
491 indicate that neurite length is dependent on BDNF concentration, with greater  
492 amounts of PODS®-rhBDNF promoting longer neurite growth (Figure 11B(a)).  
493 Lesser amounts of PODS®-rhBDNF, however, are necessary to create an ap-  
494 propriate concentration gradient. In the presence of 20,000 PODS®-rhBDNF,  
495 both neurite extension into the microchannels and cell migration into the neu-  
496 rotrophin compartment are greatest in the region closest to the BDNF source  
497 and decrease further from the PODS®-rhBDNF (Figure 11B(b,c)). Cell migra-  
498 tion is dependent on the distance from the source of BDNF, thus suggesting the  
499 presence of a BDNF gradient as predicted by our model. Note that the Xona  
500 microchannels intended to prevent from migration across channels.

501 **4. Discussion**

502 *4.1. Challenges in neurotrophin treatment in the inner ear*

503 This is a proof-of-concept study for the realization of a neurotrophic strip  
504 to ascertain its scientific/technological parameters in a controlled *in vitro* en-

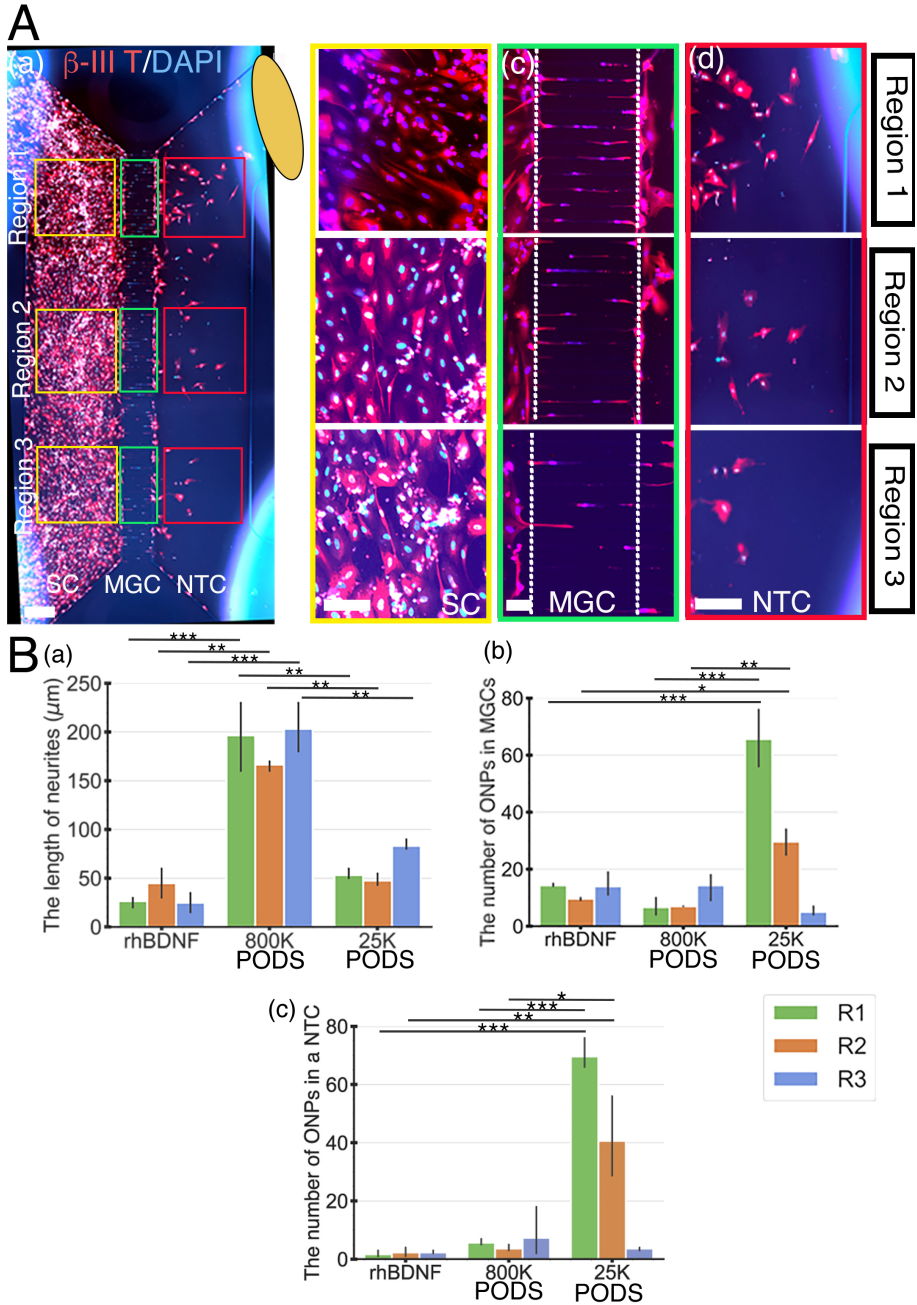


Figure 11: Human PSC-derived late-stage ONPs in the microfluidic device were stained with  $\beta$ -III tubulin (red) and DAPI (blue) to measure cell migration. (A): Late-stage ONPs stained after seven days in culture (a) with regions highlighted and magnified in the somal compartment (b), microgroove channels (c), and neurotrophin compartment (d). SC: somal compartment, MGC: microgroove channels, NTC: neurotrophic compartment. An ellipse-shaped PODS®-rhBDNF disc is shown in yellow. Scale bar (a): 500  $\mu\text{m}$ ; (b)–(d): 100  $\mu\text{m}$ . (B): Quantitative analyses of cell migration and neurite extension in devices using recombinant human BDNF, 800,000 PODS®-rhBDNF, or 20,000 PODS®-rhBDNF. \* :  $p < 0.05$ , \*\*:  $p < 0.01$ , \*\*\*:  $p < 0.001$ .

505 vironment. Neurotrophin gradients have been studied for in multiple contexts  
506 [47, 48, 49]. However, it has not been feasible to reliably provide such a gra-  
507 dient to neurons neither *in vitro* nor *in vivo*, primarily because of technical  
508 challenges. While neurotrophin treatment has been recognized as a potential  
509 treatment for sensorineural hearing loss, there has not been clinical success in  
510 this avenue to date. Most recent relevant clinical trials used adeno-associated  
511 virus (AAV2) to deliver BDNF to the brain [50]. Although exciting, this treat-  
512 ment does not attempt to control the concentration of BDNF, which could  
513 potentially interfere with normal functions in a target organ [51]. Furthermore,  
514 this treatment may not be applicable to the inner ear. In this study, we used  
515 PODS®-rhBDNF to provide a neurotrophic gradient in a controlled fashion.  
516 Our result indicated 20,000 PODS-BDNF allowed for rhBDNF neurotrophin  
517 gradient such that hESC-derived ONPs survived, differentiated toward human  
518 SGNs, and also established directional neurite outgrowth in a microfluidic device.

519 *4.2. Microfluidic device-generated gradient*

520 We used a microfluidic device to advance our understanding of directional  
521 neurite growth and otic neuronal differentiation in response to a BDNF concen-  
522 tration gradient [52]. Among many *in vitro* concentration gradient sustaining  
523 culture devices, microfluidic devices have overcome many of the deficits that  
524 conventional platforms (i.e., the Boyden chamber, Dunn chambers, or compart-  
525 mentalized diffusion chambers) face [52]. Conventional platforms tend to be sub-  
526 optimal to manipulate small volumes of fluid at the order of microliters. Growth  
527 factors and proteins are used in minute amounts in our microfluidic device, and  
528 cultured stem cells are able to interact with endogenous factors. As mentioned  
529 earlier, this micro-environment more accurately represents *in vivo* conditions.  
530 The Xona™ device can be used to sustain a three-dimensional concentration gra-  
531 dient over time (duration dependent on the half-life of the molecule) due to its  
532 microchannel array. The device limits convective flow in the gradient-forming  
533 areas by introducing microgroove channels that generate high fluidic resistance,  
534 thereby limiting flow to diffusion. The high resistance of the microchannel array

535 also prolongs diffusion across them, thereby increasing both gradient formation  
536 and gradient steepness. These features allowed us to generate a FEM, which pre-  
537 dicted the necessary number of PODS®-BDNF crystals for a BDNF gradient.  
538 Note, however, that this environment is different from the micro environment  
539 in the inner ear. A mesh geometry of the cochlea will be needed to compute the  
540 PODS®-BDNF crystal number for our next step of this study.

541 *4.3. BDNF and Polyhedrin protein*

542 Over the course of past 20–30 years, it has been established that BDNF me-  
543 diates survival and differentiation activities on SGNs by binding and activating  
544 the tyrosine kinase receptor kinase B (TrkB), a member of the larger family  
545 of Trk receptors [20]. Numerous studies have reported that BDNF can palliate  
546 SGN degeneration in ototoxically deafened animals, a widely accepted model for  
547 retrograde trans-synaptic SGN degeneration secondary to hair cell destruction  
548 [13, 14, 53, 54]. Additionally, it has been confirmed that there is a positive corre-  
549 lation between SGN counts and CI performance [55]. It is then safe to presume  
550 that treating CI recipients with BDNF would enhance overall CI performance,  
551 by preserving SGNs and their neurites. However, simply introducing rhBDNF  
552 into the inner ear poses significant hurdles. Although promising, human BDNF  
553 treatment has not been currently implemented in the inner ear. Unsuccessful  
554 BDNF treatment can be explained by several factors [56].

555 The blood half-life of BDNF protein is extremely short, only 1–10 min in  
556 the plasma [57, 58] and one hour in CSF [59]. The BDNF’s high degrada-  
557 tion rate would require continuous replenishment, impractical for clinical use.  
558 Furthermore, introduction of a homogeneous solution of BDNF would promote  
559 nondirectional neurite growth where directed neurite growth is essential for de-  
560 signing our new-generation bioactive CI, as depicted in Figure 1A. Directing  
561 neurite growth towards the CI electrode array is pivotal in the ultimate goal  
562 of enhancing performance through the narrowing of the electrode-neuron gap.  
563 The PODS® system precludes the phenomena by its localized, gradual release  
564 of growth factor. The steady supply of BDNF from a localized origin not only

565 creates a concentration gradient, but maintains it over time. As seen in Figures  
566 4–6, we were able to perform a finite element analysis based on data we collected  
567 describing the chemical release kinetics and molar ratio of PODS®-BDNF sys-  
568 tem. It is clearly visible that the slow-release nature of PODS®-BDNF results  
569 in a concentration gradient over the course of Day 1–7 (Figure 5).

570 It should be noted that our FEM assumes free diffusion of the rhBDNF  
571 protein. In biological cell-culture conditions, BDNF released from PODS®-  
572 BDNF has tendency to adhere to the walls of the culture device because BDNF  
573 is a “sticky” protein of about 27 kDa (mature BDNF dimer) and it is positively  
574 charged under physiological conditions (isoelectric point, pI = 9.4) [60]. As such,  
575 the physio-chemical properties of BDNF have made the recombinant protein  
576 difficult to diffuse. This phenomenon was observable in preliminary data where  
577 the ONPs failed to survive past 1–3 days of culture (data not shown). To  
578 circumvent this issue we infused the culture media with a carrier protein (i.e.,  
579 BSA), hypothesizing that the albumin would act as a carrier for the released  
580 BDNF and allow for free diffusion throughout the microfluidic device [61]. This  
581 hypothesis is supported by our sets of biological verification data (Figures 7–11)  
582 that clearly shows that hPSC-derived ONPs responded to the modification by  
583 exhibiting the expected cell body orientation, unidirectional neurite extension,  
584 and neurite length. Note that albumin is the single protein found in highest  
585 concentrations in the perilymph [62], therefore, a carrier protein will not be  
586 needed in our future *in vivo* study.

587 *4.4. Intracellular signaling initiated by Thyrosine kinase B receptor*

588 Another issue we need to consider in interpretation of our results is the intra-  
589 cellular cell signaling mechanism elicited by rhBDNF. Human BDNF (mature  
590 dimeric form) binds with high affinity to its TrkB receptor. The binding of  
591 BDNF to a TrkB receptor has proven to have significant importance for the  
592 proneuronal effects of BDNF [20]. Upon binding BDNF, TrkB dimerizes, and  
593 activates intrinsic kinase activities and other complex set of intracellular sig-  
594 naling cascades, which is beyond the scope of this study. However, it should

595 be noted that activation of TrkB receptor by neurotrophin binding causes the  
596 TrkB protein to be internalized in endosomes on the cellular membrane [63].  
597 Endosomes can then be transported to the soma. Therefore, the proneuronal  
598 effects of rhBDNF in our results might have highly depended on the status of  
599 TrkB receptors on the cell membrane of hPSC-derived ONPs. Our previous  
600 study has demonstrated that strong expression of a TrkB receptor on derived  
601 ONPs [24], however, more detailed studies on TrkB receptors on hPSC-derived  
602 ONP and SGNs will be needed.

603 *4.5. Degradation of PODS® crystals by protease*

604 In cell culture, degradation of PODS®-rhBDNF is likely due to the activity  
605 of cell-secreted proteases. The proteases break down the peptide bonds of the  
606 encasing polyhedrin protein, creating openings in the structure to allow release  
607 of the rhBDNF. Therefore, the presence of proteases is imperative for the proper  
608 utilization of the PODS® crystals. Additionally, these proteases are responsible  
609 for the degradation of the released BDNF. Because stem cells are not present  
610 in the culture media used for the PODS® degradation kinetics experiments, we  
611 infused the media with 10% FBS, which naturally contains proteases, to promote  
612 polyhedrin degradation, BDNF release, and BDNF degradation to attain results  
613 that more accurately describe *in vitro* events. Moreover, since the cells and  
614 PODS are initially segregated into separate compartments within the culture  
615 device, cell-secreted proteases are unlikely to reach and degrade the PODS in  
616 time to support ONP survival and differentiation. Infusion of FBS was therefore  
617 required in these experiments as well. In clinical use, however, we presume  
618 that cell-secreted proteases will be readily present in the inner ear and would  
619 therefore preclude the need for artificial supplementation.

620 *4.6. A concept design: Neurotrophic strip*

621 The plateau in CI performance in treatment of sensorineural hearing loss has  
622 driven researchers to develop innovative supplementary treatment strategies to  
623 push the field past this hurdle. Our approach strives to directly address the

624 issue at its core: the electrode-neuron gap, which can lead to serious implica-  
625 tions include low spatial frequency resolution and high power consumption. We  
626 can use our data as a launchpad for the neurotrophic strip (NS). The NS is a  
627 biointerface concept that integrates an extended-release source of growth factor  
628 to facilitate a protein gradient. Implanted in conjunction with the CI, it acts  
629 as a bridge between the extant SGNs and implanted late-ONPs grown on the  
630 electrode itself. The NS would promote survival of both cell populations, dif-  
631 ferentiation of the late ONP implants, promote directional neurite growth and  
632 synaptogenesis between the two, effectively creating a neuronal network between  
633 the patient and the implanted CI. Each electrode would be able to stimulate cell  
634 bodies at exceptionally high resolution, essential for greater intonation differ-  
635 entiability (required for effective social interaction and music appreciation) and  
636 so, increased quality of life for millions. Our successful outcomes are essential  
637 to make a neurotrophic strip feasible in *in vivo* environment.

638 *4.7. The limitations of this study and future direction*

639 There are some limitations associated with this study. First, the reduction of  
640 spacial dimension to 2D for diffusion modeling certainly affected the flux vector,  
641 which determines the predicted concentration vector. Given that the thickness  
642 (i.e., Z-axis) of the microfluidic device was 100  $\mu\text{m}$ , we estimated that the effect  
643 was minimal. In the future, we plan to use PSC-derived 3D spheroids in a somal  
644 compartment so that flux vector and concentration gradient vector can more  
645 accurately model the cell behavior. In this way, we will be able to circumvent  
646 the need to reduce diffusion calculations to 2D for computation performance in  
647 the modeling.

648 Secondly, we required to generate a model in that the BDNF's biological  
649 transportation phenomenon from a PODS<sup>®</sup>-rhBDNF disk to a somal compart-  
650 ment of a Xona<sup>™</sup> device. Note that in this model, we focused on the major  
651 dependent variable, BDNF concentration gradient to model the biological phe-  
652 nomenon. Other physical variables to promote cell migration, otic neuronal  
653 differentiation, and neurite growth were not take into consideration. These

654 variables include electotaxis (electrical potential), durotaxis (matrix's stiffness  
655 [i.e., laminin 511 in our case]) [64], mechanotaxis (cell strain), and lastly cell  
656 migration by random walk [65]. In our future study, we will take these vari-  
657 ables into consideration to more accurately represent the migration and neurite  
658 growth of hPSC-derived ONPs.

659 Insufficient contrast between cells and background in phase contrast images  
660 led to inaccuracies in cell orientation computation for some images. To address  
661 this issue, poor quality images were disregarded in the quantitative analysis.  
662 We occasionally used manual measurement for accuracy. Our future study may  
663 entail automated time-series cell analysis, which would allow more accurate  
664 measurement. Also, another way to address this issue would be with a cell  
665 membrane staining in the future.

666 While 20,000 of PODS®-rhBDNF were necessary for hPSC-derived ONPs  
667 for otic neuronal differentiation and directional neurite outgrowth, this condi-  
668 tion may not be sufficient. For instance, it is still not known whether the effects  
669 of other neurotrophic factors such as Neurotrophin-3 and Glial cell line-derived  
670 neurotrophic factor could have a positive effect on ONP growth [20, 66, 67]. We  
671 are planning to investigate these neurotrophic factors in the future. Other fac-  
672 tors that could have an impact on directional neurite growth include endogenous  
673 factors secreted from hPSC-derived ONPs. While our previous study demon-  
674 strated that hPSC-derived ONPs only secreted negligible amount of BDNF that  
675 were detected by ELISA [9], currently we do not have any data on other neu-  
676 rotrophic factors or other molecules that could have affected directional neurite  
677 growth in the inner ear. We chose BDNF first to study because the most inten-  
678 sively studied neurotrophic factor in the field of hearing research is BDNF [20].  
679 Previous studies have indicated that neurotrophic supports of SGNs are mainly  
680 from BDNF and neurotrophin-3 (NT-3) [20, 60]. Therefore, the potential con-  
681 founding effect of the secretions of other neurotrophic factors and molecules  
682 secreted from derived SGNs are likely NT-3, for which further investigation is  
683 necessary in the future.

684 Despite the aforementioned limitations associated in this study, the present

685 results generated BDNF concentration gradient, condition of which is necessary  
686 for hPSC-derived ONPs to differentiate into the otic lineage (i.e., SGNs) and  
687 also promoted directional neurite extension towards the POD-BDNF disk. The  
688 technique will allow us to control neurite direction of transplanted hPSC-derived  
689 ONPs in the inner ear. We will harness this method in our design of a bioactive  
690 CI.

691 **Conclusions**

692 We were able to generate BDNF concentration gradient, enabling survival,  
693 neuronal differentiation toward SGNs, and directed neurite extension of hPSC-  
694 derived ONPs. The technique will allow us to control neurite direction of trans-  
695 planted hPSC-derived ONPs in the inner ear. This proof-of-concept study pro-  
696 vides a step toward next-generation bioacitve CI technology.

697 **Acknowledgment**

698 This work was supported by the American Otological Society Clinician Sci-  
699 entist Award (AJM), the Triological Society/American College of Surgeons  
700 Clinician Scientist Award (AJM), the Department of Otolaryngology of North-  
701 western University (AJM), the NIH (NIDCD) K08 Clinician Scientist Award  
702 K08DC13829-02 (AJM), and the Office of the Assistant Secretary of Defense of  
703 Health Affairs through the Hearing Restoration Research Program (Award #:  
704 RH170013:WU81XWUH-18-0712). Imaging work was performed at the North-  
705 western University Center for Advanced Microscopy, which is generously sup-  
706 ported by NCI CCSG P30 CA060553 awarded to the Robert H. Lurie Com-  
707 prehensive Cancer Center, for which we thank Peter Dluhy, Constadina Ar-  
708 vanitis, Ph.D., David Kirchenbuechler, Ph.D., and Wensheng (Wilson) Liu,  
709 M.D. Some of microfluidic device experiments were performed in the Analytical  
710 bioNanoTechnology (ANTEC) Core Facility of the Simpson Querrey Institute  
711 at Northwestern University, which is supported by the Soft and Hybrid Nan-  
712 otechnology Experimental (SHyNE) Resource (NSFECCS-1542205). We thank

713 Shreyas Bharadwaj (Cornell University), Kyle Coots (Midwestern University),  
714 Andrew Oleksijew (the University of Nebraska), Duncan Chadly (California In-  
715 stitute of Technology), and Shun Kobayashi (the University of Texas at Austin)  
716 for their contribution to the earlier phases of this project. We thank Sara Dun-  
717 lop (Department of Neurology, Northwestern University), and Dr. Jacqueline  
718 Bond (the University of California San Diego) for assistance in Western Blot and  
719 SDS-Page gels. We also thank Dr. Georgia Minakaki (Department of Neurol-  
720 ogy, Northwestern University) on assistance in ELISA. Finally, our thanks and  
721 appreciation go to our collaborator, Dr. Christian Pernstich (Cell Guidance  
722 Systems), for continuous support and stimulating discussions on this project  
723 since 2015.

724 **References**

- 725 [1] J. G. Naples, M. J. Ruckenstein, Cochlear Implant., Otolaryngologic Clinics  
726 of North America 53 (1) (2020) 87–102. doi:10.1016/j.otc.2019.09.  
727 004.
- 728 [2] B. S. Wilson, M. F. Dorman, Cochlear implants: A remarkable past  
729 and a brilliant future, Hearing Research 242 (1-2) (2008) 3–21. arXiv:  
730 NIHMS150003, doi:10.1016/j.heares.2008.06.005.
- 731 [3] C. Frick, M. Müller, U. Wank, A. Tropitzsch, B. Kramer, P. Senn, H. Rask-  
732 Anderson, K. H. Wiesmüller, H. Löwenheim, Biofunctionalized peptide-  
733 based hydrogels provide permissive scaffolds to attract neurite outgrowth  
734 from spiral ganglion neurons, Colloids and Surfaces B: Biointerfaces 149  
735 (2017) 105–114. doi:10.1016/j.colsurfb.2016.10.003.
- 736 [4] S. Hahnewald, A. Tscherter, E. Marconi, J. Streit, H. R. Widmer, C. Gar-  
737 nham, H. Benav, M. Mueller, H. Löwenheim, M. Roccio, P. Senn, Response  
738 profiles of murine spiral ganglion neurons on multi-electrode arrays., Jour-  
739 nal of neural engineering 13 (1) (2016) 16011. doi:10.1088/1741-2560/  
740 13/1/016011.

- 741 [5] R. K. Shepherd, S. Hatsushika, G. M. Clark, Electrical stimulation of  
742 the auditory nerve: The effect of electrode position on neural excitation,  
743 Hearing Research 66 (1) (1993) 108–120. doi:10.1016/0378-5955(93)  
744 90265-3.
- 745 [6] M. Tykocinski, L. T. Cohen, B. C. Pyman, T. Roland, C. Treaba, J. Palamara,  
746 M. C. Dahm, R. K. Shepherd, J. Xu, R. S. Cowan, N. L. Cohen,  
747 G. M. Clark, Comparison of electrode position in the human cochlea using  
748 various perimodiolar electrode arrays., The American journal of otology  
749 21 (2) (2000) 205–211. doi:10.1016/S0196-0709(00)80010-1.
- 750 [7] A. Roemer, U. Köhl, O. Majdani, S. Klöß, C. Falk, S. Haumann, T. Lenarz,  
751 A. Kral, A. Warnecke, Biohybrid cochlear implants in human neurosensory  
752 restoration., Stem cell research and therapy 7 (1) (2016) 148. doi:10.  
753 1186/s13287-016-0408-y.
- 754 [8] R. A. Heuer, K. T. Nella, H. T. Chang, K. S. Coots, A. M. Oleksijew,  
755 C. B. Roque, L. H. Silva, T. L. McGuire, K. Homma, A. J. Matsuoka,  
756 Three-dimensional otic neuronal progenitor spheroids derived from human  
757 embryonic stem cells, Tissue Engineering - Part A 27 (3-4) (2021) 256–269.  
758 doi:10.1089/ten.tea.2020.0078.
- 759 [9] H.-T. Chang, R. A. Heuer, A. M. Oleksijew, K. S. Coots, C. B. Roque, K. T.  
760 Nella, T. L. McGuire, A. J. Matsuoka, An Engineered Three-Dimensional  
761 Stem Cell Niche in the Inner Ear by Applying a Nanofibrillar Cellulose  
762 Hydrogel with a Sustained-Release Neurotrophic Factor Delivery System,  
763 Acta Biomaterialia 108 (2020) 111–127. doi:<https://doi.org/10.1016/j.actbio.2020.03.007>.
- 764 [10] L. Taylor, L. Jones, M. H. Tuszyński, A. Blesch, Neurotrophin-3 gradients  
765 established by lentiviral gene delivery promote short-distance axonal bridg-  
766 ing beyond cellular grafts in the injured spinal cord, Journal of Neuroscience  
767 26 (38) (2006) 9713–9721. doi:10.1523/JNEUROSCI.0734-06.2006.

- 769 [11] P. Senn, M. Roccio, S. Hahnewald, C. Frick, M. Kwiatkowska, M. Ishikawa,  
770 P. Bako, H. Li, F. Edin, W. Liu, H. Rask-Andersen, I. Pyykkö, J. Zou,  
771 M. Mannerström, H. Keppner, A. Homsy, E. Laux, M. Llera, J. P. Lel-  
772 louche, S. Ostrovsky, E. Banin, A. Gedanken, N. Perkas, U. Wank, K. H.  
773 Wiesmüller, P. Mistrík, H. Benav, C. Garnham, C. Jolly, F. Gander, P. Ul-  
774 rich, M. Müller, H. Löwenheim, NANOCI-Nanotechnology Based Cochlear  
775 Implant with Gapless Interface to Auditory Neurons, *Otology and Neuro-*  
776 *urology* 38 (8) (2017) e224—e231. doi:10.1097/MAO.0000000000001439.
- 777 [12] G. J. Goodhill, H. Baier, Axon Guidance: Stretching Gradients to  
778 the Limit, *Neural Computation* 10 (3) (1998) 521–527. doi:10.1162/  
779 089976698300017638.
- 780 [13] L. N. Gillespie, G. M. Clark, P. F. Bartlett, P. L. Marzella, BDNF-induced  
781 survival of auditory neurons *in vivo*: Cessation of treatment leads to ac-  
782 celerated loss of survival effects, *Journal of Neuroscience Research* 71 (6)  
783 (2003) 785–790. doi:10.1002/jnr.10542.
- 784 [14] L. N. Pettingill, R. L. Minter, R. K. Shepherd, Schwann cells geneti-  
785 cally modified to express neurotrophins promote spiral ganglion neuron  
786 survival *in vitro*, *Neuroscience* 152 (3) (2008) 821–828. doi:10.1016/j.  
787 *neuroscience*.2007.11.057.Schwann.
- 788 [15] R. K. Shepherd, A. Coco, S. B. Epp, Neurotrophins and electrical stim-  
789 ulation for protection and repair of spiral ganglion neurons following  
790 sensorineural hearing loss, *Hearing Research* 242 (2009) 100–109. doi:  
791 10.1016/j.heares.2007.12.005.Neurotrophins.
- 792 [16] B. Baseri, J. J. Choi, T. Deffieux, G. Samiotaki, Y. S. Tung, O. Olu-  
793 molade, S. A. Small, B. Morrison, E. E. Konofagou, Activation of sig-  
794 naling pathways following localized delivery of systemically administered  
795 neurotrophic factors across the bloodbrain barrier using focused ultra-  
796 sound and microbubbles, *Physics in Medicine and Biology* 57 (7). doi:  
797 10.1088/0031-9155/57/7/N65.

- 798 [17] K. Ikeda, S. Nagaoka, S. Winkler, K. Kotani, H. Yagi, K. Nakanishi,  
799 S. Miyajima, J. Kobayashi, H. Mori, Molecular Characterization of Bom-  
800 byx mori Cytoplasmic Polyhedrosis Virus Genome Segment 4, *Journal of*  
801 *Virology* 75 (2) (2001) 988–995. doi:[10.1128/jvi.75.2.988-995.2001](https://doi.org/10.1128/jvi.75.2.988-995.2001).
- 802 [18] T. Suzuki, T. Kanaya, H. Okazaki, K. Ogawa, A. Usami, H. Watanabe,  
803 K. Kadono-Okuda, M. Yamakawa, H. Sato, H. Mori, S. Takahashi, K. Oda,  
804 Efficient protein production using a Bombyx mori nuclear polyhedrosis  
805 virus lacking the cysteine proteinase gene, *Journal of General Virology*  
806 78 (12) (1997) 3073–3080. doi:[10.1099/0022-1317-78-12-3073](https://doi.org/10.1099/0022-1317-78-12-3073).
- 807 [19] H. Mori, R. Ito, H. Nakazawa, M. Sumida, F. Matsubara, Y. Minobe,  
808 Expression of Bombyx mori cytoplasmic polyhedrosis virus polyhedrin in  
809 insect cells by using a baculovirus expression vector, and its assembly into  
810 polyhedra, *Journal of General Virology* 74 (1) (1993) 99–102. doi:[10.1099/0022-1317-74-1-99](https://doi.org/10.1099/0022-1317-74-1-99).
- 812 [20] S. H. Green, E. Bailey, Q. Wang, R. L. Davis, The Trk A, B, C's of  
813 Neurotrophins in the Cochlea., *Anatomical record* (Hoboken, N.J. : 2007)  
814 295 (11) (2012) 1877–1895. doi:[10.1002/ar.22587](https://doi.org/10.1002/ar.22587).
- 815 [21] I. Meyvantsson, D. J. Beebe, Cell culture models in microfluidic systems,  
816 *Annual Review of Analytical Chemistry* 1 (1) (2008) 423–449. doi:[10.1146/annurev.anchem.1.031207.113042](https://doi.org/10.1146/annurev.anchem.1.031207.113042).
- 818 [22] Z.-J. Guo, M.-H. Yu, X.-Y. Dong, W.-L. Wang, T. Tian, X.-Y. Yu, X.-D.  
819 Tang, Protein composition analysis of polyhedra matrix of Bombyx mori  
820 nucleopolyhedrovirus (BmNPV) showed powerful capacity of polyhedra to  
821 encapsulate foreign proteins., *Scientific reports* 7 (1) (2017) 8768. doi:  
822 [10.1038/s41598-017-08987-8](https://doi.org/10.1038/s41598-017-08987-8).
- 823 [23] A. J. Matsuoka, Z. A. Sayed, N. Stephanopoulos, E. J. Berns, A. R. Wad-  
824 hwani, Z. D. Morrissey, D. M. Chadly, S. Kobayashi, A. N. Edelbrock,  
825 T. Mashimo, C. A. Miller, T. L. McGuire, S. I. Stupp, J. A. Kessler,

- 826      Creating a stem cell niche in the inner ear using self-assembling peptide  
827      amphiphiles., Plos One 12 (12) (2017) e0190150. doi:10.1371/journal.  
828      pone.0190150.
- 829      [24] A. J. Matsuoka, Z. D. Morrissey, C. Zhang, K. Homma, A. Belmadani,  
830      C. A. Miller, D. M. Chadly, S. Kobayashi, A. N. Edelbrock, M. Tanaka-  
831      Matakatsu, D. S. Whitlon, L. Lyass, T. L. McGruire, S. I. Stupp, J. A.  
832      Kessler, Directed Differentiation of Human Embryonic Stem Cells Toward  
833      Placode-Derived Spiral Ganglion-Like Sensory Neurons, Stem Cells Trans-  
834      lational Medicine 6 (2017) 923–936. doi:10.1002/sctm.16-0032.
- 835      [25] H. Al-Ali, S. R. Beckerman, J. L. Bixby, V. P. Lemmon, In vitro models  
836      of axon regeneration, Experimental Neurology 287 (Pt 3) (2017) 423–434.  
837      doi:10.1016/j.expneurol.2016.01.020.
- 838      [26] U. K. Laemmli, Cleavage of structural proteins during the assembly of  
839      the head of bacteriophage T4., Nature 227 (5259) (1970) 680–685. doi:  
840      10.1038/227680a0.
- 841      [27] A. L. Mandel, H. Ozdener, V. Utermohlen, Identification of pro- and mature  
842      brain-derived neurotrophic factor in human saliva., Archives of oral biology  
843      54 (7) (2009) 689–695. doi:10.1016/j.archoralbio.2009.04.005.
- 844      [28] C. A. Schneider, W. S. Rasband, K. W. Eliceiri, NIH Image to ImageJ:  
845      25 years of image analysis, Nature Methods 9 (7) (2012) 671–675. arXiv:  
846      arXiv:1011.1669v3, doi:10.1038/nmeth.2089.
- 847      [29] R. W. Burry, Controls for immunocytochemistry: an update., The journal  
848      of histochemistry and cytochemistry : official journal of the Histochemistry  
849      Society 59 (1) (2011) 6–12. doi:10.1369/jhc.2010.956920.
- 850      [30] M. B. Mazalan, M. A. B. Ramlan, J. H. Shin, T. Ohashi, Effect of geomet-  
851      ric curvature on collective cell migration in tortuous microchannel devices,  
852      Micromachines 11 (7) (2020) 1–17. doi:10.3390/MI11070659.

- 853 [31] F. Xu, T. Beyazoglu, E. Hefner, U. A. Gurkan, U. Demirci, Automated  
854 and adaptable quantification of cellular alignment from microscopic images  
855 for tissue engineering applications, *Tissue Engineering - Part C: Methods*  
856 17 (6) (2011) 641–649. doi:[10.1089/ten.tec.2011.0038](https://doi.org/10.1089/ten.tec.2011.0038).
- 857 [32] E. Batschelet, *Circular Statistics in Biology (Mathmatics in Biology Series)*,  
858 1st Edition, Academic Press, New York, NY, 1981.
- 859 [33] P. Berens, M. J. Velasco, CircStat for Matlab: Toolbox for circular statistics  
860 with Matlab, Max–Planck–Institut f ur biologische Kybernetik, Technical  
861 Report No. 184 31 (10) (2009) 1–21. doi:[doi:10.18637/jss.v031.i10](https://doi.org/10.18637/jss.v031.i10).
- 862 [34] M. Pool, J. Thiemann, A. Bar-Or, A. E. Fournier, NeuriteTracer: A novel  
863 ImageJ plugin for automated quantification of neurite outgrowth, *Journal*  
864 of Neuroscience Methods 168 (1) (2008) 134–139. doi:[10.1016/j.jneumeth.2007.08.029](https://doi.org/10.1016/j.jneumeth.2007.08.029).
- 866 [35] E. Meijering, M. Jacob, J.-C. F. Sarria, P. Steiner, H. Hirling, M. Unser,  
867 Design and validation of a tool for neurite tracing and analysis in fluo-  
868 rescence microscopy images., *Cytometry. Part A : the journal of the In-*  
869 *ternational Society for Analytical Cytology* 58 (2) (2004) 167–176. doi:  
870 [10.1002/cyto.a.20022](https://doi.org/10.1002/cyto.a.20022).
- 871 [36] M. Anniko, W. Arnold, T. Stigbrand, A. Strom, The Human Spiral Gan-  
872 glion, *ORL* 57 (1995) 68–77.
- 873 [37] S. van der Walt, S. C. Colbert, G. Varoquaux, The NumPy Array: A  
874 Structure for Efficient Numerical Computation, *Computing in Science En-*  
875 *gineering* 13 (2) (2011) 22–30. doi:[10.1109/MCSE.2011.37](https://doi.org/10.1109/MCSE.2011.37).
- 876 [38] J. D. Hunter, Matplotlib: A 2D Graphics Environment, *Computing in*  
877 *Science Engineering* 9 (3) (2007) 90–95. doi:[10.1109/MCSE.2007.55](https://doi.org/10.1109/MCSE.2007.55).
- 878 [39] P. Virtanen, R. Gommers, T. E. Oliphant, M. Haberland, T. Reddy,  
879 D. Cournapeau, E. Burovski, P. Peterson, W. Weckesser, J. Bright, S. J.

- van der Walt, M. Brett, J. Wilson, K. J. Millman, N. Mayorov, A. R. J. Nelson, E. Jones, R. Kern, E. Larson, C. J. Carey, I. Polat, Y. Feng, E. W. Moore, J. VanderPlas, D. Laxalde, J. Perktold, R. Cimrman, I. Henriksen, E. A. Quintero, C. R. Harris, A. M. Archibald, A. H. Ribeiro, F. Pedregosa, P. van Mulbregt, SciPy 1.0: fundamental algorithms for scientific computing in Python., *Nature methods* 17 (3) (2020) 261–272.  
[doi:10.1038/s41592-019-0686-2](https://doi.org/10.1038/s41592-019-0686-2).
- [40] P. Berens, CircStat : A MATLAB Toolbox for Circular Statistics , *Journal of Statistical Software* 31 (10). [doi:10.18637/jss.v031.i10](https://doi.org/10.18637/jss.v031.i10).
- [41] M. Tuncel, H. S. Sürücü, K. M. Erbil, A. Konan, Formation of the cochlear nerve in the modiolus of the guinea pig and human cochleae., *Archives of medical research* 36 (5) (2005) 436–40. [doi:10.1016/j.arcmed.2005.02.003](https://doi.org/10.1016/j.arcmed.2005.02.003).
- [42] B. Küçük, K. Abe, T. Ushiki, Y. Inuyama, S. Fukuda, Kazuo Ishikawa, Microstructures of the Bony Modiolus in the Human Cochlea : A Scanning Electron Microscopic Study, *Journal of Electron Microsc* 40 (40) (1991) 193–197.
- [43] O. Levenspiel, Chemical Reaction Engineering, 3rd Edition, John Wiley and Sons, Inc., New York, NY, 1999.
- [44] M. Stroh, W. R. Zipfel, R. M. Williams, S. C. Ma, W. W. Webb, W. M. Saltzman, Multiphoton microscopy guides neurotrophin modification with poly(ethylene glycol) to enhance interstitial diffusion, *Nature Materials* 3 (7) (2004) 489–494. [doi:10.1038/nmat1159](https://doi.org/10.1038/nmat1159).
- [45] S. Axler, Linear Algebra Done Right, 3rd Edition, Springer Publishing, New York, NY, 2015.
- [46] J. Crank, The mathematics of Diffusion, 2nd Edition, Oxford University Press, London, UK, 1979.

- 907 [47] K. M. Keefe, I. S. Sheikh, G. M. Smith, Targeting Neurotrophins to Specific  
908 Populations of Neurons: NGF, BDNF, and NT-3 and Their Relevance  
909 for Treatment of Spinal Cord Injury., International journal of molecular  
910 sciences 18 (3). doi:10.3390/ijms18030548.
- 911 [48] B. I. Awad, M. A. Carmody, M. P. Steinmetz, Potential role of growth  
912 factors in the management of spinal cord injury., World Neurosurgery 83 (1)  
913 (2015) 120–131. doi:10.1016/j.wneu.2013.01.042.
- 914 [49] E. R. n. Hollis, M. H. Tuszyński, Neurotrophins: potential therapeutic tools  
915 for the treatment of spinal cord injury., Neurotherapeutics : the journal of  
916 the American Society for Experimental NeuroTherapeutics 8 (4) (2011)  
917 694–703. doi:10.1007/s13311-011-0074-9.
- 918 [50] A. H. Nagahara, B. R. Wilson, I. Ivasyk, I. Kovacs, S. Rawalji, J. R.  
919 Bringas, P. J. Piviroto, W. S. Sebastian, L. Samaranch, K. S. Bankiewicz,  
920 M. H. Tuszyński, MR-guided delivery of AAV2-BDNF into the entorhi-  
921 nal cortex of non-human primates., Gene therapy 25 (2) (2018) 104–114.  
922 doi:10.1038/s41434-018-0010-2.
- 923 [51] S. D. Croll, C. Suri, D. L. Compton, M. V. Simmons, G. D. Yan-  
924 copoulos, R. M. Lindsay, S. J. Wiegand, J. S. Rudge, H. E. Scharfman,  
925 Brain-derived neurotrophic factor transgenic mice exhibit passive avoid-  
926 ance deficits, increased seizure severity and in vitro hyperexcitability in  
927 the hippocampus and entorhinal cortex., Neuroscience 93 (4) (1999) 1491–  
928 1506. doi:10.1016/s0306-4522(99)00296-1.
- 929 [52] A. Dravid, S. Parittotokkaporn, Z. Aqrawe, S. J. O’Carroll, D. Svirskis,  
930 Determining Neurotrophin Gradients in Vitro to Direct Axonal Outgrowth  
931 following Spinal Cord Injury, ACS Chemical Neuroscience 11 (2) (2020)  
932 121–132. doi:10.1021/acschemnuro.9b00565.
- 933 [53] T. Yamagata, J. M. Miller, M. Ulfendahl, N. P. Olivius, R. A. Altschuler,  
934 I. Pyykkö, G. Bredberg, Delayed neurotrophic treatment preserves nerve

- 935 survival and electrophysiological responsiveness in neomycin-deafened  
936 guinea pigs., Journal of neuroscience research 78 (1) (2004) 75–86. doi:  
937 10.1002/jnr.20239.
- 938 [54] M. P. Zanin, M. Hellstr??m, R. K. Shepherd, A. R. Harvey, L. N. Gillespie,  
939 Development of a cell-based treatment for long-term neurotrophin expres-  
940 sion and spiral ganglion neuron survival, Neuroscience 277 (2014) 690–699.  
941 doi:10.1016/j.neuroscience.2014.07.044.
- 942 [55] M. Seyyedi, L. Viana, J. J. Nadol, Within-subject comparison of word  
943 recognition and spiral ganglion cell count in bilateral cochlear implant  
944 recipients, Otol Neurotol 35 (8) (2014) 1446–1450. doi:10.1097/MAO.  
945 000000000000443.Within-Subject.
- 946 [56] A. Henriques, C. Pitzer, A. Schneider, Neurotrophic growth factors for the  
947 treatment of amyotrophic lateral sclerosis: where do we stand?, Frontiers  
948 in neuroscience 4 (2010) 32. doi:10.3389/fnins.2010.00032.
- 949 [57] J. F. Poduslo, G. L. Curran, Permeability at the blood-brain and  
950 blood-nerve barriers of the neurotrophic factors: NGF, CNTF, NT-3,  
951 BDNF, Molecular Brain Research 36 (2) (1996) 280–286. doi:10.1016/  
952 0169-328X(95)00250-V.
- 953 [58] T. Sakane, W. M. Pardridge, Carboxyl-directed pegylation of brain-derived  
954 neurotrophic factor markedly reduces systemic clearance with minimal loss  
955 of biologic activity (1997). doi:10.1023/A:1012117815460.
- 956 [59] R. G. Soderquist, E. D. Milligan, E. M. Sloane, J. A. Harrison, K. K.  
957 Douvas, J. M. Potter, T. S. Hughes, R. A. Chavez, K. Johnson, L. R.  
958 Watkins, M. J. Mahoney, PEGylation of brain-derived neurotrophic factor  
959 for preserved biological activity and enhanced spinal cord distribution.,  
960 Journal of biomedical materials research. Part A 91 (3) (2009) 719–729.  
961 doi:10.1002/jbm.a.32254.

- 962 [60] M. Sasi, B. Vignoli, M. Canossa, R. Blum, Neurobiology of local and inter-  
963 cellular BDNF signaling, *Pflugers Archiv : European journal of physiology*  
964 469 (5-6) (2017) 593–610. doi:10.1007/s00424-017-1964-4.
- 965 [61] X. Li, Y. Su, S. Liu, L. Tan, X. Mo, S. Ramakrishna, Encapsulation  
966 of proteins in poly(l-lactide-co-caprolactone) fibers by emulsion electro-  
967 spinning, *Colloids and Surfaces B: Biointerfaces* 75 (2) (2010) 418–424.  
968 doi:10.1016/j.colsurfb.2009.09.014.
- 969 [62] E. E. L. Swan, M. Peppi, Z. Chen, K. M. Green, J. E. Evans, M. J.  
970 McKenna, M. J. Mescher, S. G. Kujawa, W. F. Sewell, Proteomics analysis  
971 of perilymph and cerebrospinal fluid in mouse., *The Laryngoscope* 119 (5)  
972 (2009) 953–958. doi:10.1002/lary.20209.
- 973 [63] T. Numakawa, S. Suzuki, E. Kumamaru, N. Adachi, M. Richards,  
974 H. Kunugi, BDNF function and intracellular signaling in neurons, *Histology  
975 and Histopathology* 25 (2) (2010) 237–258. doi:10.14670/HH-25.237.
- 976 [64] C. Gentile, Engineering of Spheroids for Stem Cell Technology, *Current  
977 Stem Cell Research & Therapy* 11 (2016) 652–665. doi:10.2174/  
978 1574888x10666151001114848.
- 979 [65] H. Berg, *Random Walks in Biology*, Princeton Universtiyy Press, Prinston,  
980 NJ, 1983.
- 981 [66] H. Li, F. Edin, H. Hayashi, O. Gudjonsson, N. Danckwardt-Lillies, H. En-  
982 gqvist, H. Rask-Andersen, W. Xia, Guided growth of auditory neurons:  
983 Bioactive particles towards gapless neural electrode interface, *Biomaterials*  
984 122 (2017) 1–9. doi:10.1016/j.biomaterials.2016.12.020.
- 985 [67] J. Schulze, H. Staeker, D. Wedekind, T. Lenarz, A. Warnecke, Expression  
986 pattern of brain-derived neurotrophic factor and its associated receptors:  
987 Implications for exogenous neurotrophin application., *Hearing Research* 413  
988 (2020) 108098. doi:10.1016/j.heares.2020.108098.